# Geophysical Journal International

# 3-D *P*-wave velocity structure of oceanic core complexes at 13°N on the Mid-Atlantic Ridge

N.M. Simão,[1] C. Peirce [ORCID],[1] M.J. Funnell,[1] A.H. Robinson,[1] R.C. Searle,[1] C.J. MacLeod[2] and T.J. Reston[3]

[1]*Department of Earth Sciences, Durham University, South Road, Durham, DH13LE, UK. E-mail: christine.peirce@durham.ac.uk*
[2]*School of Earth and Ocean Sciences, Cardiff University, Park Place, Cardiff, CF103AT, UK*
[3]*School of Geography, Earth and Environmental Sciences, University of Birmingham, Edgbaston, Birmingham, B152TT, UK*

## SUMMARY

The Mid-Atlantic Ridge at 13°N is regarded as a type locality for oceanic core complexes (OCCs), as it contains, within ∼70 km along the spreading axis, four that are at different stages of their life cycle. The wealth of existing seabed observations and sampling makes this an ideal target to resolve contradictions between the existing models of OCC development. Here we describe the results of *P*-wave seismic tomographic modelling within a 60 × 60 km footprint, containing several OCCs, the ridge axis and both flanks, which determines OCC crustal structure, detachment geometry and OCC interconnectivity along axis. A grid of wide-angle seismic refraction data was acquired along a series of 17 transects within which a network of 46 ocean-bottom seismographs was deployed. Approximately 130 000 first arrival traveltimes, together with sparse Moho reflections, have been modelled, constraining the crust and uppermost mantle to a depth of ∼10 km below sea level. Depth slices through this 3-D model reveal several independent structures each with a higher *P*-wave velocity ($Vp$) than its surrounds. At the seafloor, these features correspond to the OCCs adjacent to the axial valley walls at 13°20′N and 13°30′N, and off axis at 13°25′N. These high-$Vp$ features display dipping trends into the deeper crust, consistent with the surface expression of each OCC's detachment, implying that rocks of the mid-to-lower crust and uppermost mantle within the footwall are juxtaposed against lower $Vp$ material in the hangingwall. The neovolcanic zone of the ridge axis has systematically lower $Vp$ than the surrounding crust at all depths, and is wider between OCCs. On average, throughout the 13°N region, the crust is ∼6 km-thick. However, beneath a deep lava-floored basin between axial OCCs the crust is thinner and is more characteristically oceanic in layering and velocity–depth structure. Thicker crust at the ridge axis suggests a more magmatic phase of current crustal formation, while modelling of the sparse Moho reflections suggests the crust–mantle boundary is a transition zone throughout most of the 13°N segment. Our results support a model in which OCCs are bounded by independent detachment faults whose dip increases with depth and is variable with azimuth around each OCC, suggesting a geometry and mechanism of faulting that is more complicated than previously thought. The steepness of the northern flank of the 13°20′N detachment suggests that it represents a transfer zone between different faulting regimes to the south and north. We propose that individual detachments may not be linked along-axis, and that OCCs act as transfer zones linking areas of normal spreading and detachment faulting. Along ridge variation in magma supply influences the nature of this detachment faulting. Consequently, not only does magma supply control how detachments rotate and migrate off axis before finally becoming inactive, but also how, when and where new OCCs are created.

**Key words:** Controlled source seismology; Crustal imaging; Crustal structure; Mid-ocean ridge processes.

# 1 INTRODUCTION

Slow-spreading ridges are traditionally characterized by a volcanic axial valley bounded by a symmetric set of inward-facing, low-offset normal faults. The valley width and the amount of slip along the valley wall faults are controlled by the degree of magmatism which, in turn, is influenced by the rate of spreading (Lin *et al.* 1990; Detrick *et al.* 1995; Thibaud *et al.* 1998). However, the discovery of both mantle rocks at the seafloor (e.g. Cannat 1993, 1996; Tucholke & Lin 1994; Cannat *et al.* 1995, 1997; Lagabrielle *et al.* 1998) and the identification of gently dipping, corrugated surfaces (termed oceanic core complexes—OCCs) at the slow-spreading Mid-Atlantic Ridge (e.g. Cann *et al.* 1997; Blackman *et al.* 1998; Tucholke *et al.* 1998; MacLeod *et al.* 2002; Reston *et al.* 2002; Tivey *et al.* 2003; Dannowski *et al.* 2010), at the ultraslow-spreading South West Indian Ridge (e.g. Searle *et al.* 2003; Baines *et al.* 2008; Sauter *et al.* 2013) and elsewhere (e.g. Ohara *et al.* 2001; Okino *et al.* 2004; Sato *et al.* 2009; Hayman *et al.* 2011), has revealed that the axial valley model is far from representative of the interplay between and diversity of tectonic and magmatic processes occurring at slower spreading rates.

Seismic and sampling studies have revealed that OCC footwalls contain gabbroic rocks typical of newly accreted magmatic crust (e.g. Escartín *et al.* 2003a; Ildefonse *et al.* 2007; Canales *et al.* 2008; Dick *et al.* 2008; Planert *et al.* 2010), which numerical modelling has additionally shown can form under moderate-to-high regional magmatic conditions (Buck *et al.* 2005; Tucholke *et al.* 2008; Olive *et al.* 2010). However, serpentinites, which reflect hydrothermally altered rocks of the lower crust/upper mantle, are also commonly sampled on OCC detachment surfaces (Escartín *et al.* 1997, 2003a; Canales *et al.* 2004; Picazo *et al.* 2012; Hansen *et al.* 2013). These large-scale fault surfaces have been interpreted as the source of deep, high-angle, normal seismicity (e.g. deMartin *et al.* 2007), and are shown by palaeomagnetic studies to undergo significant footwall rotation close to the surface (e.g. Grimes *et al.* 2008; Morris *et al.* 2009; MacLeod *et al.* 2011). These observations support a model in which the curved, convex-up, gently-sloping OCC detachment steepens with depth due to flexural rotation (e.g. Buck 1988; Reston & Ranero 2011), and along which rocks of the deeper crust and upper mantle are exhumed to shallowest crustal depths (Escartín & Canales 2011).

Hydrothermal activity is also often associated with detachment faulting, with slope-failure surfaces and associated extensional fractures and fissures providing high permeability pathways for hydrothermal fluids to percolate into the fault hangingwall and footwall (e.g. Axen 1992; Canales *et al.* 2007; Dunn *et al.* 2017). The location of hydrothermal vents off axis appears dependent on the life-stage of the detachment, and their existence dependent on a heat source at depth to drive the fluid flow (e.g. Gràcia *et al.* 2000; Früh-Green *et al.* 2003; McCaig *et al.* 2007; Ondréas *et al.* 2012).

OCC detachments asymmetrically accommodate much of the plate separation, significantly influencing the ridge morphology (e.g. Escartín *et al.* 2008; Smith *et al.* 2008; Schouten *et al.* 2010; Simão *et al.* 2010; Grevemeyer *et al.* 2013). Two models have been proposed to explain their origin and subsequent evolution. In the *segment-scale* model, OCCs are viewed as the surface expression of a continuous segment-scale detachment, which is covered in the intervening regions by a thin veneer of rider blocks of volcanic seafloor (Reston & Ranero 2011). In this model, detachments are considered to be long-lived features, and asymmetric spreading occurs along the entire segment length (e.g. Escartín *et al.* 2008). In the alternative *local-scale* model, OCCs are viewed as spatially restricted, relatively short-lived features, with fault initiation and slip dependent on variation in local magma supply (e.g. MacLeod *et al.* 2009; Mallows & Searle 2012). In this model, detachments are seen as ordinary valley-wall faults along which slip continues until the magmatic conditions change (e.g. Howell *et al.* 2016, 2019). Spreading is locally strongly asymmetric between an OCC and its conjugate ridge flank, but not along the entire length of the spreading segment (e.g. MacLeod *et al.* 2009).

The existing models are largely unconstrained by direct observations at depth. Although observations to date (e.g. deMartin *et al.* 2007) suggest that detachments flatten abruptly upwards to follow a shallower, gently dipping trend, these existing studies have been unable to directly image the detachment at depth or its roll-over. They are, therefore, unable to ascertain any continuity between steeply and shallowly dipping zones, nor show the lateral extent of the detachment and, thus, connectivity between OCCs at depth.

The 13°N region of the Mid-Atlantic Ridge (hereafter 13°N; Fig. 1) is regarded as a type locality for OCCs, and provides the observational basis upon which the *segment-scale* and *local-scale* models were developed. It contains four OCCs within an ∼70 km section along the west flank of the spreading axis, all of which are at various stages of their life cycle (e.g. Smith *et al.* 2006; MacLeod *et al.* 2009). Given the wealth of existing seabed morphological observations and lithology sampling, 13°N therefore represents an ideal target to resolve the contradictions between the existing evolutionary models, by imaging their subsurface crustal structure to determine the geometry and lateral connectivity of the detachment with depth.

To investigate the subsurface structure and tectonic processes of the 13°N OCCs, three research expeditions were undertaken on the RRS James Cook between 2014 and 2016:

(i) JC102 and JC109–Peirce (2014a, b)—which undertook a passive ocean-bottom seismograph deployment and recovery to record local microseismicity, the results of which have been reported by Parnell-Turner *et al.* (2017) and

(ii) JC132–Reston & Peirce (2016)—which undertook active-source seismic (wide-angle refraction and multichannel reflection), and shipboard gravity, magnetic and swath bathymetry imaging, together with autonomous underwater vehicle near-seabed swath bathymetry and magnetic surveying. The combined shipboard and near-seabed magnetics were reported by Searle *et al.* (2016), and their detailed analysis is discussed in Searle *et al.* (2018). A 2-D, south–north seismic and gravity transect through Marathon fracture zone (Fig. 1) and the 13°20′N (hereafter 1320) and 13°30′N (hereafter 1330) OCCs is described by Peirce *et al.* (2019).

Here we describe the results of *P*-wave seismic tomographic modelling within a 60 × 60 km footprint crustal volume (hereafter the 3-D grid—Fig. 2). This contains two OCCs near the ridge axis (1320 and 1330) and a relict OCC preserved off axis at 13°25′N (hereafter 1325), together with the ridge axis and both ridge flanks. Our aim was to determine OCC crustal structure, detachment geometry and OCC interconnectivity along axis in three-dimensions from seabed to uppermost mantle depth.

# 2 STUDY AREA

The 13°N study area is located in the tropical Atlantic (Fig. 1) and has a complex tectonic history associated with movement of the boundaries between the North American, South American and African plates and the opening of the Atlantic Ocean (Escartín *et al.*
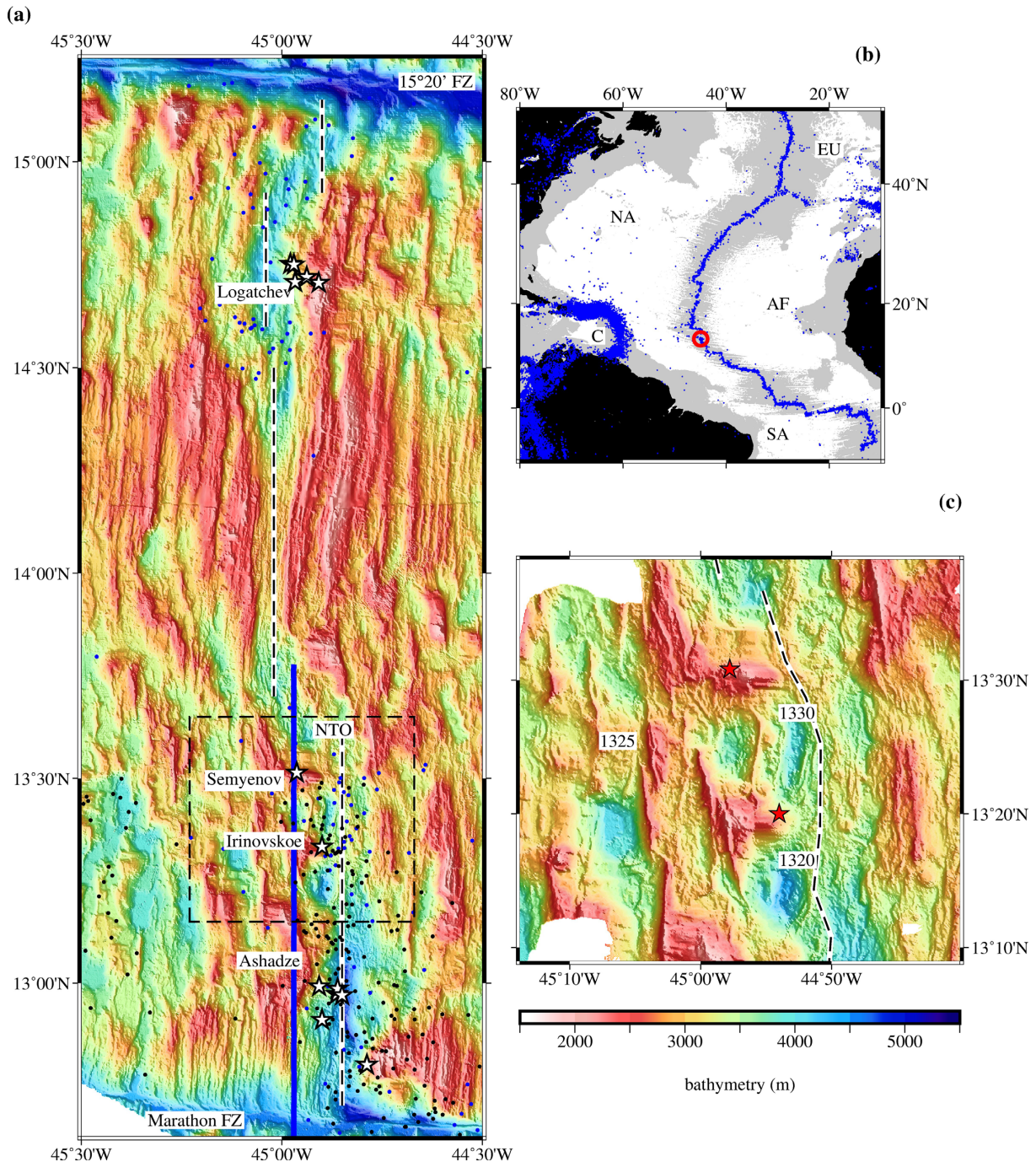
**Figure 1.** The 13°N and 14°N segments of the MAR. (a) Regional swath bathymetry (100 m resolution) between the Marathon and 15°20′N fracture zones showing the ridge-parallel normal faulting of the magmatic region to the north of the non-transform offset (NTO) located at 13°35′N, and the OCC-hosting terrane of the western ridge flank to the south. The Logatchev, Semyenov, Irinovskoe and Ashadze active hydrothermal vents sites are marked by white stars. Black dashed lines indicate the generalized location of the ridge axis, the blue line Profile R of Peirce *et al.* (2019) and the black dashed box the 13°N 3-D grid region shown in Fig. 2. A 13°N subset of hydroacoustically detected seismicity is marked by black-filled dots (e.g. Smith *et al.* 2003, 2006; Escartín *et al.* 2003b) and blue-filled dots mark earthquake epicentres from the USGS Earthquake Hazards Program catalogue (https://earthquake.usgs.gov). (b) Plate boundaries in the central Atlantic as marked by earthquake epicentres, with the 13°N study area marked by the red circle. EU—Eurasia; NA—North America; AF—Africa; C—Caribbean; SA—South America plates. The location of the boundary between the North America and South America plates is debated. (c) Local swath bathymetry (20 m resolution) of the 13°N 3-D grid study area showing the morphology of labelled OCCs. Red stars mark active vent sites. Black dashed line shows the Mallows & Searle (2012) average ridge axis location. The same bathymetry colour scale is used in all other bathymetry figures.

2003b and references therein). Although the North America–South America plate boundary is typically associated with the 15°20′N fracture zone (FZ, Fig. 1a), there is little seismicity associated with it, unlike the plate boundary between Africa and Eurasia (Fig. 1b).

There is also no fault network or fracture zone connecting it to the Caribbean plate. Instead, a sparse band of off axis seismicity, running parallel to the MAR ridge axis between 13°N and 14°N (Fig. 1b), suggests a more complex and/or diffuse plate boundary
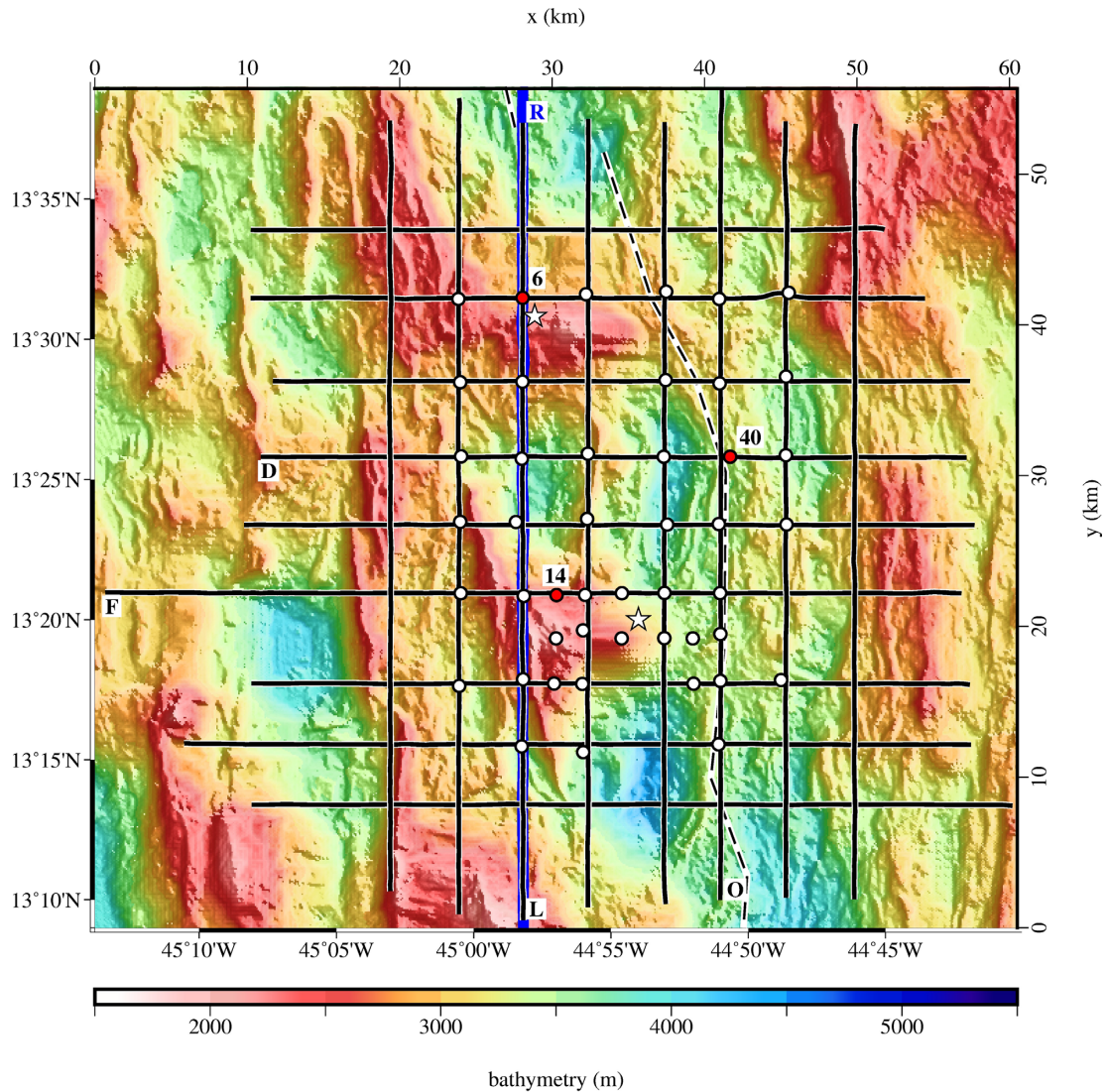
**Figure 2.** 13°N 3-D grid acquisition layout. Both latitude–longitude and *x*–*y* grids are indicated. Seventeen seismic shot profiles are shown by the solid black lines with example profile names labelled. OBS locations are marked by white circles. Red circles show the locations of OBSs whose record sections are shown in Figs 3 and 4. White stars mark vent sites and the black dashed line Mallows & Searle's (2012) average ridge axis. Profile R (Peirce *et al.* 2019) is located by the thick blue line (*cf.* Fig. 1a) and is coincident with Profile L of the 3-D grid.

and the possibility of past ridge jumps (Escartín *et al.* 2003b). Mallows & Searle (2012) found that striations on the OCC on the east flank at 13°48′N, believed to mark the fault slip direction, matched North America–Africa plate motion, whereas similar striations on 1330 and 1320 matched South America–Africa plate motion.

To the east of the band of seismicity lies the 13°N segment that apparently comprises sections undergoing magmatic spreading intertwined with regions undergoing predominantly tectonic extension that contain the OCCs. This along-ridge variation in spreading style results in a wider ridge axis neovolcanic zone in the magmatic sections and an asymmetric increase in fault heave on the western flank associated with the OCCs (Smith *et al.* 2008; MacLeod *et al.* 2009; Mallows & Searle 2012). The seafloor morphology within the tectonic sections also shows that significant mass wasting occurs (Cannat *et al.* 2013; Escartín *et al.* 2017). The precise position of the ridge axis is unclear. Mallows & Searle (2012) provide four different estimates, differing by up to 10 km east–west, depending on data type considered (bathymetry, gravity, magnetic field or acoustic backscatter). Here we adopt their average position (Fig. 1c)**.**

The 13°N segment is bounded to the south by the Marathon FZ and to the north by a non-transform offset (NTO) located at ∼13°35′N (Fig. 1a). The 14°N MAR segment to the north of this NTO has a geochemical anomaly characteristic of large volume, high temperature melting and results in symmetric abyssal hill normal faulting and an unusually thick igneous crust, that is indicated by an anomalously low mantle Bouguer anomaly (MBA–Dosso *et al.* 1991; Bonatti *et al.* 1992; Escartín & Cannat 1999; Fujiwara *et al.* 2003). This MBA gradually increases along-ridge to the south, from its regional minimum that lies within the 14°N MAR segment (Fujiwara *et al.* 2003).

The OCCs of the 13°N segment, as well as the 13°48′N OCC on the opposing east flank, have all been well studied during the past 10 yr. Recent near-seabed magnetic anomaly observations surrounding the 1320 and 1330 OCCs have revealed a strong negative magnetization (especially at 1320) that is attributed to relatively old, reversely magnetized lithosphere that has been exhumed along the detachment fault (Searle *et al.* 2018). A passive microseismicity study has shown that the 1320 OCC footwall is being deformed

by compressive stresses caused by the detachment's roll-over before reaching the seafloor (Parnell-Turner *et al.* 2017), while other studies have shown that hydrothermal systems preferentially use the detachments as permeability conduits (Ondréas *et al.* 2012; Picazo *et al.* 2012; Escartín *et al.* 2017). By enabling silica-rich fluids to flow into the bounding ultramafic rocks, these systems influence the depth of the brittle–plastic transition as well as the types of deformation that occur. Pervasive silicification of the 1320 OCC detachment surface (Bonnemains *et al.* 2017) supports the concept that shallow, low-angle dipping detachments are capable of producing ∼5 $M_w$ earthquakes and are, therefore, stronger than previously thought (Craig & Parnell-Turner 2017).

The 13°N region is home to three active vent localities (Fig. 1a):

(i) Ashadze—a set of black smokers located along the western axial valley wall associated with detachment faulting;
(ii) Irinovskoe—a black smoker system located close to the seafloor hangingwall cut-off of the 1320 OCC and
(iii) Semyenov—a white smoker located in the chaotic seabed terrain northwest of the corrugated surface of the 1330 OCC.

The Semyenov white smoker active vent site is located ∼10 km off axis [using the Mallows & Searle (2012) average ridge axis location] and away from the OCC corrugated surface (Figs 1a and c). Adopting the McCaig *et al.* (2007) criteria, the vent type and location imply that the 1330 OCC is at the end of its life-cycle or already inactive. Conversely, the black smokers of Irinovskoe (located close to the 1320 OCC footwall–hangingwall border) and Ashadze, imply that these active vents are located on a mature detachment. In the case of the Irinovskoe vent site in particular, it is located too far from the detachment fault trace to result from fluid flow along it and, instead, implies the existence of the magmatic pluton within the crust beneath it (McCaig *et al.* 2007).

Studies of the seabed expression of the detachment fault zone reveal that surface processes like mass wasting, erosion and blanketing by an apron of hangingwall-derived material influences the seafloor morphology (Cannat *et al.* 2013; Escartín *et al.* 2017; Olive *et al.* 2019), and that a detachment may represent a linkage between different fractures that coalesce, giving rise to the characteristic corrugations of the domed surfaces (Parnell-Turner *et al.* 2018a). Finally, Parnell-Turner *et al.*'s (2018b) study of the 13°48′N OCC on the eastern flank suggests that detachments continue to slip after episodes of magmatic intrusion, which Howell *et al.* (2019) demonstrate by numerical modelling using the 1320 OCC as an example.

The OCCs of the 13°N segment have become a type site for study because they share these characteristics with many other OCCs studied along the MAR (e.g. Smith *et al.* 2008; Picazo *et al.* 2012; Parnell-Turner *et al.* 2018a, Olive *et al.* 2019). However, despite a considerable number of studies having been conducted at 13°N, little is known about the subseabed crustal structure. This study focuses on the 3-D grid area located between 13°10′N and 13°40′N (Fig. 2) that contains the 1320, 1325 and 1330 OCCs; 1320 is thought to be still active, while 1330 is thought to have been active until recently in geological terms (MacLeod *et al.* 2009; Mallows & Searle 2012), while the 1325 OCC is relict and now preserved ∼25 km off axis in the ∼2-Myr-old lithosphere of the western ridge flank.

## 3  DATA ACQUISITION

Wide-angle (WA) seismic refraction data were acquired along a series of 17 transects in the form of a grid (Fig. 2), within which a

dense network of 46 ocean-bottom seismographs (OBSs) was deployed. Each OBS was equipped with a three-component (*x*, *y*, *z*) geophone set and a hydrophone. Data were recorded at a sampling rate of 250 Hz over 60 s trace lengths to match the shot firing rate, which resulted in an intershot interval of ∼150 m at a mean survey speed of 4.9 kn (2.5 m s$^{-1}$). This approach enabled continuous recording between OBS deployment and recovery, so that microseismic events would also be recorded during non-shooting periods to extend the Parnell-Turner *et al.* (2017) analysis over a much broader region. The results of this microseismicity study will be reported separately.

The seismic source consisted of an array of 13 Bolt airguns with a total volume of 4800 in$^3$ (78.7 l), towed at a depth of ∼8 m. Each OBS was relocated to its true seafloor position by forward ray trace modelling of water-wave traveltimes using *rayinvr* (Zelt & Ellis 1988; Zelt & Smith 1992) and a model of the water column constructed from sound velocity profiles measured throughout the study area. This water column model was used for all subsequent subseabed arrival traveltime modelling.

Prior to traveltime picking, the OBS data were filtered with a bandpass 5–20 Hz filter to remove the background swell and seabed scattered noise. *P*-wave first arrivals for the crust (Pg) and mantle (Pn), and reflected arrivals from the Moho (PmP), were picked using either the vertical geophone or hydrophone channel, depending on whichever had the highest signal-to-noise ratio for each deployment site. Approximately 130 000 first arrival traveltimes were picked, with pick uncertainties of between 50 and 75 ms assigned based on shot and instrument location errors and the signal-to-noise ratio, the latter of which correlates with source–receiver offset. While Moho reflections are observed on some record sections, they are few in number (total of ∼600 picks). Example record sections for OBSs 40 (ridge axis—Profiles D and O; Fig. 3), 06 (1330 OCC—Profile L; Figs 4a and b) and 14 (1320 OCC—Profile F; Figs 4d and e) show the observed phase identifications, picks and pick errors, and that arrivals are generally observed to a distance of ∼30 km from each OBS. The seabed topography throughout the study area strongly influences first arrival trend. Although the inter-OBS spacing varies between ∼2 and 5 km, the shot spacing along profile provides short offset, shallower propagating ray paths with which to constrain the uppermost crust (Figs 3c and f).

## 4  TOMOGRAPHIC INVERSION

### 4.1  Modelling procedure and parametrization

Traveltime inversion was conducted using *FAST* (First Arrival Seismic Tomography–Zelt and Barton 1998), which applies a regularized inversion method to fitting modelled to observed traveltimes. The laterally variable (between ∼1.85 and 4.35 km) model seabed interface was created by sampling the bathymetry at each forward grid cell spacing, and projecting these and the OBS and shot locations into kilometre-space relative to a model 0,0 located at 13°09.0′N/45°13.8′W. The seabed interface, which mirrors the seabed topography throughout the 3-D grid, remained fixed throughout modelling.

A two-pronged approach to modelling was adopted. The density of ray paths in the upper crust enabled a higher resolution model (henceforth termed the *Higher Resolution Shallow Model—HRSM*) to be obtained for the upper-to-mid crust by setting the regular Cartesian grid forward node spacing at 0.25 km, both laterally and vertically, and by setting the inverse cell size, which controls the
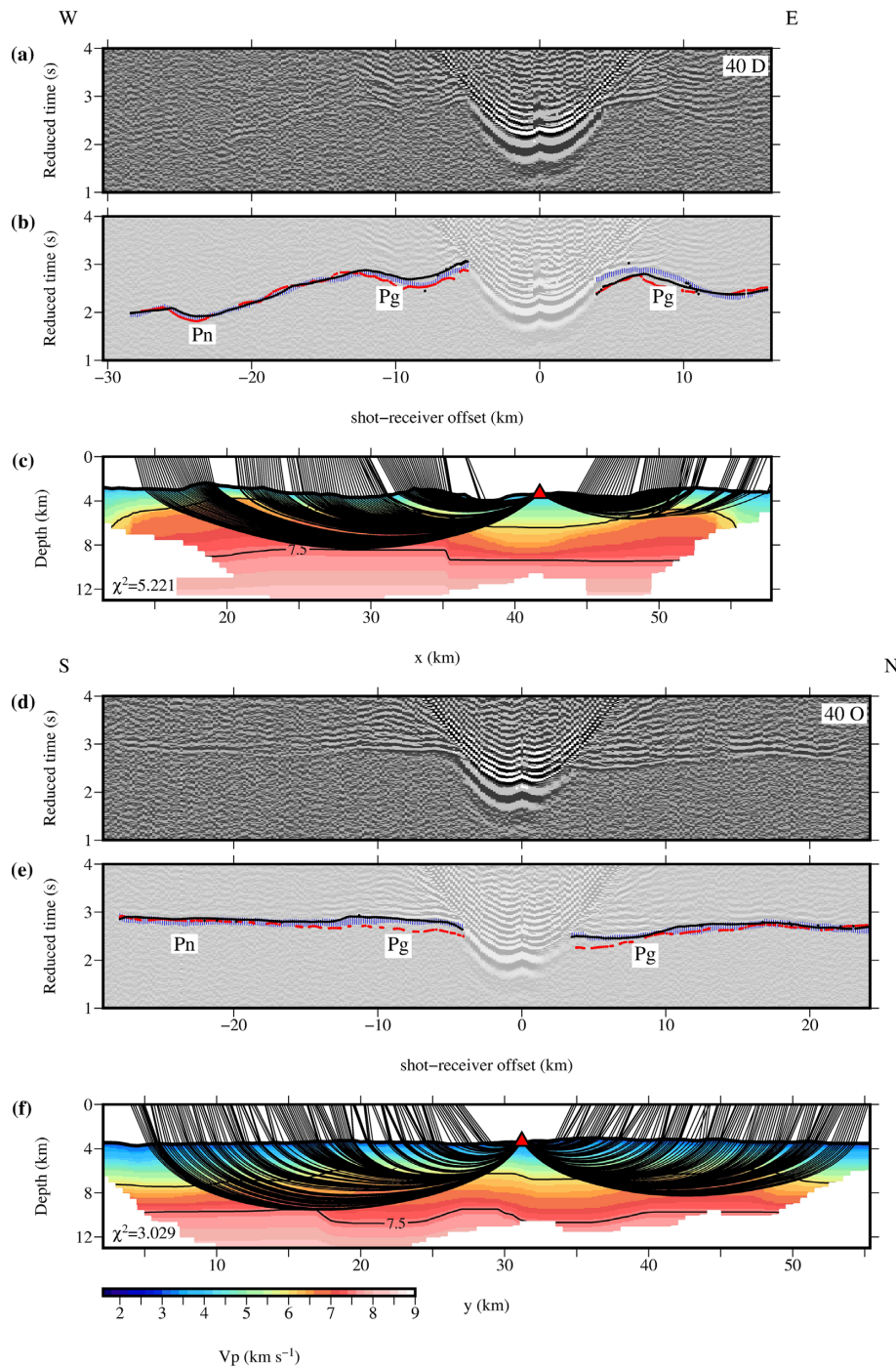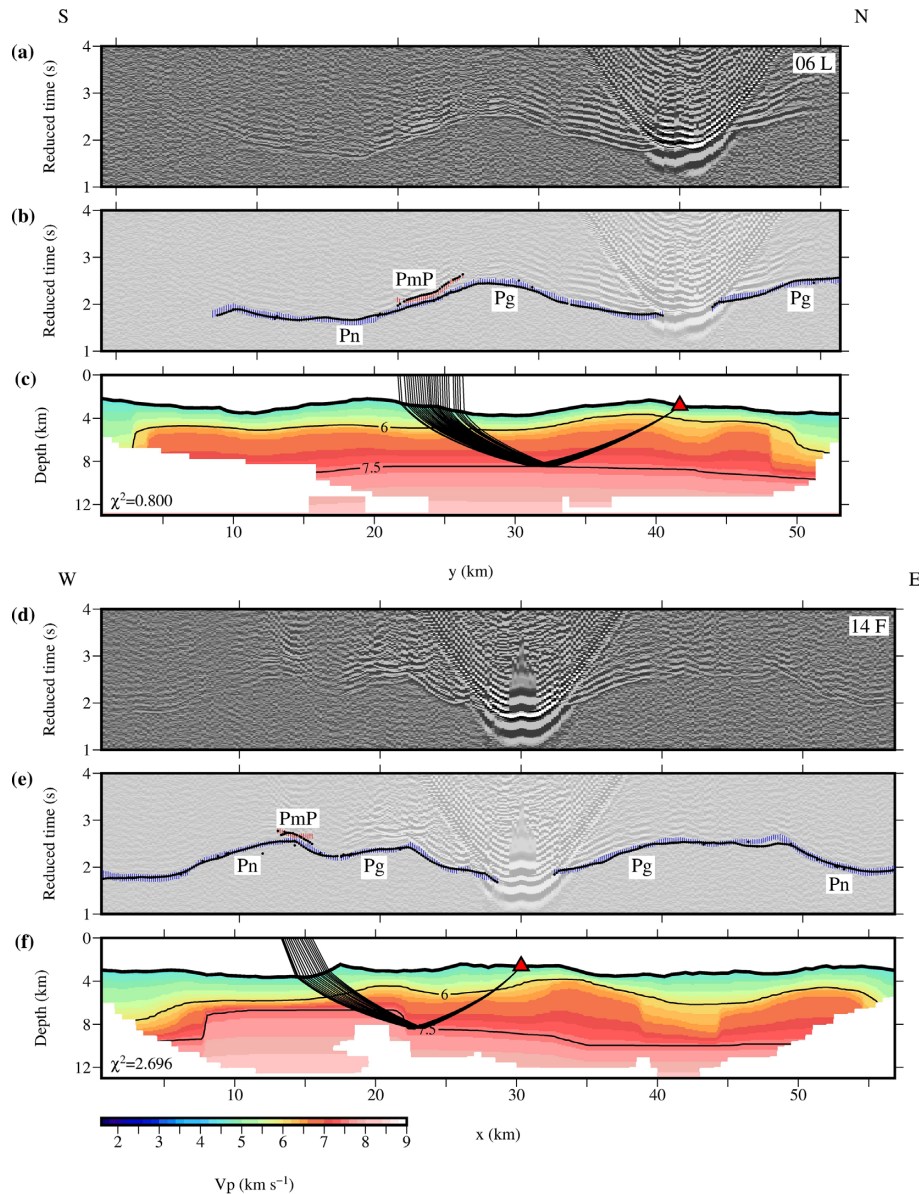
**Figure 3.** Example hydrophone record sections for OBS 40, displayed with a bandpass 5–20 Hz filter. All record sections are plotted with a reduction velocity of 6 km s$^{-1}$. (a) Profile D shots and (b) record section from (a) with first arrival traveltime picks plotted as blue bars, whose length corresponds to assigned pick uncertainty of 50–75 ms. Calculated traveltimes from the 3-D inversion are shown by black dots. Traveltimes calculated by forward ray tracing through a 2-D model derived from the *inversion model* are marked by red dots. See text for details on model construction. The geometry of first arrival trend is predominantly influenced by the seabed topography. Pg—crustal refracted arrival; Pn—mantle refracted arrival. (c) Ray paths forward-traced through a 2-D node-based model representation of the *inversion model* sliced along Profile D. (d–f) Equivalent for Profile O. Parts (c) and (f) are masked by the *inversion model* ray coverage. See Fig. 2 for profile and OBS locations.

scales over which the model smoothing is applied, to 0.75 km laterally and 0.25 km vertically. A second model (henceforth termed the *Lower Resolution Deep Model—LRDM*) was parametrized with a 0.5 km (laterally and vertically) forward node spacing and a 1.5 km lateral by 0.5 km vertical inverse cell size, which provided sufficient ray coverage in each cell to determine the velocity structure throughout the entire crust and uppermost mantle. The forward and inverse grid node spacings were chosen as that which resulted in a sufficient and even cell hit count distribution, considering the acquisition geometry and the variation in seabed topography.

The outcome of an inversion is dependent on the traveltime picks, the initial model and the smoothing parameters. Therefore, 100

**Figure 4.** Example hydrophone record sections for OBSs 06 and 14, displayed with a bandpass 5–20 Hz filter. All record sections are plotted with a reduction velocity of 6 km s⁻¹. (a and b) OBS 06 for Profile L shots with first arrival traveltime picks plotted as blue bars and Moho reflections as red bars in (b), with length corresponding to assigned pick uncertainty of 50–75 ms. Pg—crustal refracted arrival; Pn—mantle refracted arrival; PmP—Moho reflection. First arrival traveltimes calculated from the *inversion model* (Fig. 5) are shown as black dots. Moho reflections were calculated by forward ray tracing through a 2-D node-based representation of *inversion model* sliced along Profile L. (c) P-wave velocity structure along Profile L, with forward-traced ray paths of PmP arrivals compared to those recorded by OBS 06. These arrivals are due to a high velocity gradient boundary between crust and mantle. (d–f) Equivalent for OBS 14 along Profile F. See Fig. 2 for profile and OBS locations. Parts (c) and (f) are masked using the *inversion model* ray coverage.

1-D initial models were developed and inverted for each model parametrization to determine the best fit (Fig. S1). These starting models incorporated a fixed minimum velocity of 2.5 km s⁻¹ at the mean seabed depth (2.9 km), and a maximum velocity of 9.0 km s⁻¹ at 12 km depth (approximating the seismic velocity of olivine formed at 200 MPa–Miller and Christensen 1997), with varying increases in velocity applied between these two values (Figs S1a and d). Each initial model was configured to have a linearly increasing velocity with depth parallel to the sea surface rather than seabed. This approach avoided inclusion of any preconceived seabed-following layered velocity structure as might be expected for normal magmatic oceanic crust. If such a structure resulted from the inversion it would be required by the data and, thus, enable

magmatic and exhumed regions of crust to be distinguished with confidence.

Each initial model was inverted over a series of six iterations, with six values of the trade-off parameter (λ), which controls the balance between minimizing the data misfit and generating a model with the minimum required structure, tested for each iteration. The initial value of λ (lambda0) was randomly assigned as either 20, 50 or 100, and the smoothness factor (Sz), which determines the importance of maintaining the vertical versus horizontal smoothness, was randomly chosen within the range recommended for a 3-D inversion by Zelt & Barton (1998).

The parameters of the best-fitting model inversions are summarized in Table 1, and were selected based on the minimization of the

**Table 1.** Regularized inversion parameters for the best-fitting models.

| Model | Forward spacing (km) | Inverse spacing (km) | Trade-off parameter, $\lambda$ | Smoothness factor, Sz | $\chi^2$ |
|---|---|---|---|---|---|
| 1 | $0.25^{hv}$ | $0.75^{h} / 0.25^{v}$ | 1.25 | 0.125 | 1.00 |
| 2 | $0.50^{hv}$ | $1.50^{h} / 0.50^{v}$ | 0.44 | 0.125 | 1.26 |

*h*—horizontal spacing; *v*—vertical spacing.

misfit and the extent to which artefacts were introduced into the resulting model (Fig. S2). The selected initial models are highlighted in Figs S1(a) and (d), a vertical slice through the initial model for *HRSM* is shown in Fig. 5(b), and the traveltime residuals for both the *HRSM* and *LRDM* are shown in Figs S1(b), (c), (e) and (f). The $\chi^2$ fits for these models (0.997 and 1.261, respectively) demonstrate that they are a good fit to the observed traveltime picks, using the $\chi^2 = 1$ criterion to describe fit to within pick error. Figs S1(c) and (f) also show that the misfit residual for each model is independent of offset (except for picks made from parts of records sections showing much higher background noise levels). The *LRDM* is considered to be a good fit for the entire crust and uppermost mantle, and the *HRSM* a good fit for the upper crust to a depth of up to 6 km below sea level (bsl).

## 4.2 Resolution

In order to test both the lateral and depth resolution of the best-fitting models, the checkerboard approach of Zelt (1998) was followed. A ±5 per cent velocity perturbation checkerboard pattern was added to each model with different checkerboard dimensions. Permutations of 2, 3, 5 and 10 km checkerboard dimensions in the *x* and *y* directions and 1 and 2 km in the *z* direction were tested, together with shifts in the phase of the applied pattern of a half and a full wavelength in each of the three directions. Synthetic traveltimes were calculated for each of these perturbed models, using the shot-receiver offsets of the observed traveltime picks. Gaussian random noise was then added to the synthetic traveltimes, with values corresponding to the pick uncertainties. These synthetic picks were inverted using each best-fitting model as the starting point, and using the same parameters (Table 1) and number of iterations. The resulting checkerboard inversions range in $\chi^2$ between 1.02 and 1.06.

The degree of recovery, defined by the semblance (Zelt 1998), was subsequently determined by comparing the recovered perturbation pattern to that imposed on each model. To take account of potential pattern geometry dependence on outcome, the semblance for all patterns within each checkerboard permutation were averaged (Figs S4–S7). We adopt Zelt's (1998) semblance threshold of 0.7 to define areas of the model that are well resolved, even though semblance can be misleading as it is dependent on the operator radius. For each pattern tested, we use an operator radius set to the horizontal checkerboard cell size.

In the region surrounding the 1320 OCC (Fig. 2), checkerboard testing demonstrates that the *HRSM* is able to resolve structures as small as 2 × 2 × 1 km to a depth of ∼4 km bsl in the region surrounding the OCCs (insets to Figs S4b–d), due to the higher density of OBSs surrounding this OCC. For the 3-D grid as a whole, the *HRSM* is capable of resolving 3 × 3 × 2 km structures to 6 km bsl (Figs S4b–h). However, the *HRSM* fails to resolve the crust–mantle transition due to reduced ray coverage below 6 km-depth.

In contrast, the smoother *LRDM* does not resolve small-scale features in the shallowest part of the crust (Fig. S6), as a result of its larger forward node and inverse cell size. Resolution testing of the *LRDM* shows, however, that this configuration is still able to resolve features as small as 3 × 3 × 2 km to 7 km bsl in the centre of the 3-D grid (insets to Figs S6b–d), and 5 × 5 × 2 km generally throughout the crust. At depths >7 km bsl, the *LRDM* can only resolve features larger than 10 × 10 × 2 km to a maximum depth of 10 km bsl beneath the centre of the OBS array (Figs S6e–h). Between 10 and 50 km in both the *x* and *y* directions, the *HRSM* and *LRDM* only differ in absolute velocity terms by less than 0.125 km s$^{-1}$ at all depths.

Our testing indicates that not only is each OCC well resolved throughout the crust, but so are the regions in between and surrounding these OCCs together with the ridge axis. The latter thus enables investigation of the ridge axis location [*cf.* Mallows & Searle's (2012) definition] and foci of any geologically recent magmatism as implied from Searle *et al.*'s (2018) magnetics study.

## 4.3 Crust–mantle boundary

*FAST* (Zelt & Barton 1998) uses first arrival traveltimes to construct velocity models that are inherently smooth and interface-free. Consequently, to investigate the nature of the crust–mantle transition the *HRSM* and *LRDM* were merged along a common boundary at 6 km-depth bsl between 25 km and 50 km in both *x* and *y* directions, to create the *inversion model*. This model was then sliced vertically along each 2-D shot profile (Figs 2–4) and converted into a forward node-specified model with distinct layer boundaries incorporated. The 6.0 km s$^{-1}$ velocity contour was used to define the intracrustal upper-to-lower crustal boundary and the 7.5 km s$^{-1}$ velocity contour was used to represent the base of crust (Figs 3c, f and 4c, f) consistent with the result of modelling Profile R (Figs 1a and 2—Peirce *et al.* 2019). The observed traveltime picks (Pg and Pn phases) were then point-to-point ray traced using *rayinvr* (Zelt & Ellis 1988; Zelt & Smith 1992) to test model construction. Examples for OBS 40 (Profiles D and O) are shown in Figs 3(c), (f) and OBS 06 (Profile L) and OBS 14 (Profile F) are shown in Figs 4(b) and (e), with the ray-tracing resulting in a $\chi^2$ fit of <3 when averaged for all OBSs. This *forward model* was thus deemed suitable for testing the nature and location of the base of the crust.

The sparse observation of PmP phases throughout the 3-D grid footprint suggests that a distinct Moho interface does not exist, with there instead being a transition zone from crust to mantle. Consequently, a forward predictive ray tracing approach, tracing all potential PmP arrivals through the model was adopted, not only to further test the appropriateness of the selected base of crust marker (7.5 km s$^{-1}$ velocity contour), but also the likelihood that it is a distinct interface rather than a transition zone and, if so, where it exists.

Modelled reflections mirror PmP phases on the record sections (Figs 4b, c and e, f) where they are observed. The implication of this result is that, elsewhere, either there is not a distinct Moho between crust and mantle, with it instead being a transition zone, or that the velocity contrast across the Moho is small. The latter would generate
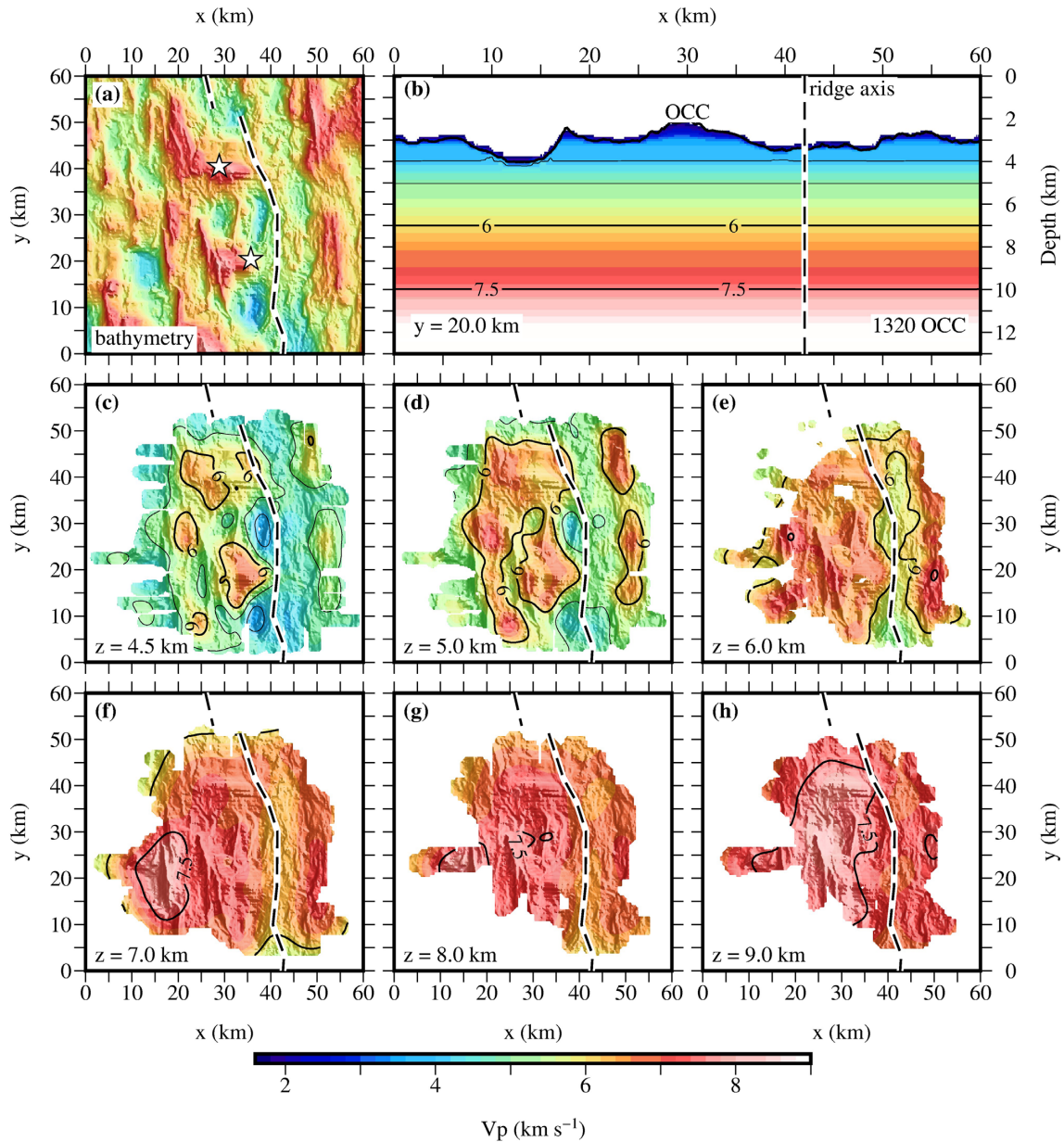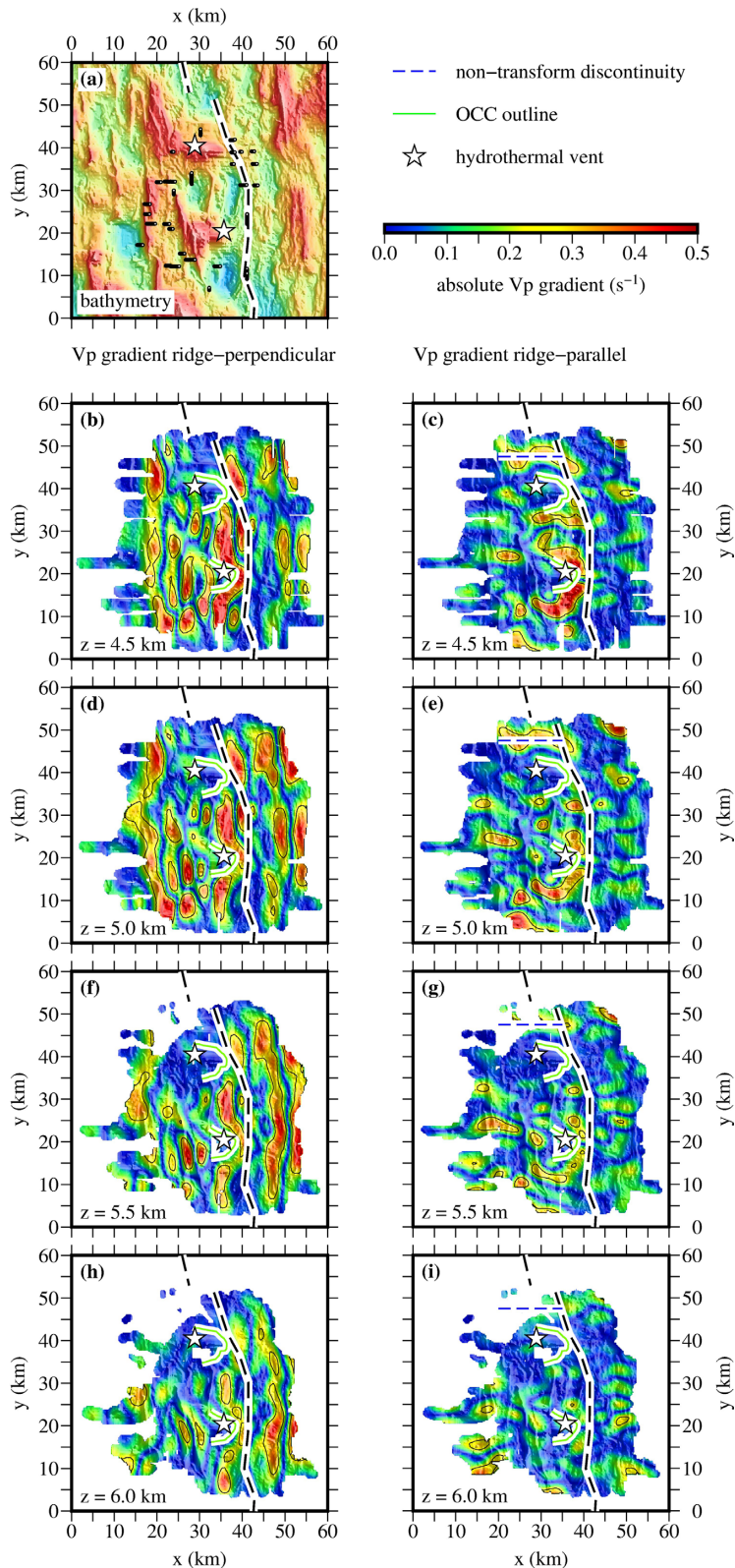
**Figure 5.** Horizontal (depth) slices through the inversion *HRSM* and *LRDM*. (a) Bathymetry showing the location of Mallows & Searle's (2012) average ridge axis (black dashed line in all parts) and the vent sites (white stars). (b) Vertical slice across axis through the initial model for 1320 OCC (at model $y = 20.0$ km) showing the 1-D velocity–depth structure starting point of the inversion of *HRSM*. The ridge axis is marked by the vertical black dashed line. Slices at (c) 4.5 km, (d) 5.0 km and (e) 6.0 km bsl through the *HRSM*, which has a resolution of $2 \times 2 \times 1$ km to a depth of $\sim$5 km bsl, and at (f) 7.0 km, (g) 8.0 km and (h) 9.0 km bsl through the *LRDM*, which has a resolution of $3 \times 3 \times 2$ km to a depth of $\sim$7 km bsl. The 6.0 km s$^{-1}$ and 7.5 km s$^{-1}$ contours, used as proxies for the upper-to-lower crust and crust-to-mantle transitions, respectively, are shown by contour lines. The 1320, 1325 and 1330 OCCs correspond to higher velocity anomalies relative to the surrounding crust, and the ridge axis is marked by a north–south trending band of lower velocity. Parts (c–h) are masked using the *inversion model* ray coverage and are illuminated by the seabed topography. An unilluminated version of this figure is provided as Fig. S3.

a low amplitude PmP arrival that would be indistinguishable above the level of the background noise. Consequently, we conclude that the 7.5 km s$^{-1}$ contour can be regarded as a proxy for the base of the crust where a distinct Moho exists and the top of a gradient transition into the mantle where it does not.

### 4.4 *Vp* gradient

An alternative approach that assists understanding of the features within the crust of the 13°N *inversion model* is the calculation of

the ridge-perpendicular and ridge-parallel horizontal gradients in *Vp* (after Dunn *et al.* 2017; Fig. 6). Using this approach, magmatically accreted upper crust shows a higher *Vp* gradient change with depth due to the crust's vertically layered lithological structure, whilst deeper crust and uppermost mantle material exhumed to the seabed, or to shallow depths, shows a low lateral gradient (e.g. the contrasting structures between the OCCs and the intervening region as shown in Figs 6b–d). Furthermore, crust resulting from magmatic accretion retains a more ridge-parallel trend in velocity structure, while the toe of each OCC (where the detachment breaks

**Figure 6.** Lateral variation in horizontal velocity gradient calculated ridge-perpendicular (left-hand column) and ridge-parallel (right-hand column). (a) Bathymetry showing the location of Mallows & Searle's (2012) average ridge axis (black dashed line in all parts) and the vent sites (white stars). PmP reflection points calculated by 2-D forward ray tracing (Fig. 4) are shown by black lines. (b–c) Velocity gradient calculated at 4.5 km bsl through the *HRSM*. The OCCs are marked by low lateral gradients which suggests that they are underlain predominantly by rocks from the lower crust and uppermost mantle. In between OCCs a high lateral gradient with a ridge-parallel alignment suggests areas where the crust has been predominantly magmatically accreted (left-hand column), and denote the OCC hangingwall (right-hand column). A steep east–west trending gradient also locates the NTO (blue dashed line). Equivalent for (d–e) 5.0 km, (f–g) 5.5 km, (h–i) 6.0 km bsl. The latter shows the ridge-parallel structure (h) of the upper crust on the eastern flank in particular. Parts (b–i) are masked using the *inversion model* ray coverage, are illuminated by the seabed topography and have the outlines of the 1320 and 1330 OCCs marked by green lines.

the seabed—known as the hangingwall cut-off) is marked by a band of higher gradient on the hangingwall side, particularly so in the ridge-perpendicular gradient given their generally arcuate shape. The NTO, which bounds the 13°N segment to the north, is also demarked in the ridge-parallel gradient at $y = 50$ km, displaying a lateral offset of 15–20 km (e.g. Figs 6c–g).

# 5 MODELLING RESULTS

The *inversion model* constrains the crust and uppermost mantle to a depth of up to 10 km bsl (Fig. 5). In order to highlight lateral velocity variation, we also consider the difference (henceforth the *difference model*) between the *inversion model* and a reference crustal structure constructed by sampling the velocity–depth structure at the ridge axis (at 40,32–Fig. 7a). This location is in between the 1320 and 1330 OCCs, in a region where the seabed comprises lava flows and volcanic edifices. This 1-D ridge axis magmatic crust reference was draped beneath the seabed interface to create the *reference model* for the entire 3-D grid. Consequently, subtraction of this model from the *inversion model* highlights where within the 3-D grid the crustal structure differs from that expected to result from normal magmatic accretion (Figs 7c–h).

## 5.1 Shallow to mid-crust–4 to 6 km bsl

The upper crust is well constrained by the *HRSM*. The horizontal (depth) slice through this model at 4.5 km (Fig. 5c) reveals three independent structures each having a higher ($>6.0$ km s$^{-1}$) $Vp$ than the surrounding region, which has a relatively low $Vp$ of $< 4.0$ km s$^{-1}$. These features continue, with higher velocities, to 5 and 6 km bsl (Figs 5d and e). At the seafloor, the three higher $Vp$ features correspond to the locations of the 1320 (at 35,20 model $x,y$) and 1330 (35,40) OCCs adjacent to the axial valley walls, and the off axis 1325 OCC (20,30). These features are well resolved, as their lateral dimensions are larger than the smallest resolvable checkerboard size of $2 \times 2 \times 1$ km, with each showing a semblance above the 0.7 threshold (Figs S4c and d insets). Furthermore, these features are not considered to be artefacts of the seafloor topography, as they display a dipping trend, steeper than the seabed topography, into the deeper crust when viewed in vertical slices through the model (Figs 8b–g), consistent with the surface expression of the detachment of each. This implies that higher velocity material of the middle-to-lower crust and even uppermost mantle exists within the footwall, and is juxtaposed against lower velocity material forming the hangingwall of each detachment (*cf*. Figs 8b–c and f–g).

Vertical slices through the *HRSM* show that, away from the OCCs, the *P*-wave velocity of the shallow crust rapidly increases from 2.5 km s$^{-1}$ at the seafloor to 6.0 km s$^{-1}$ at ∼2.0 km below the seafloor (Fig. 8). This steep velocity gradient correlates with where seafloor samples imply the crust comprises lava flows and pillow lavas overlying a sheeted dyke complex (MacLeod *et al.* 2009; Mallows & Searle 2012), normally associated with oceanic crust layer 2 (White *et al.* 1992; Grevemeyer *et al.* 2018).

The thickness of the upper crust was calculated (Fig. 9e), using the change in velocity gradient with depth marked by the 6.0 km s$^{-1}$ contour as a proxy for its base. In general, off axis the upper crust is ∼2 km thick, with the western flank ∼10–20 per cent thinner than the eastern. The low $Vp$ anomaly that extends to 6 km bsl at the ridge axis implies that the upper crust is much thicker (up to 3 km thick) there than anywhere else (Fig. 9e), and that the Mallows &

Searle (2012) average definition of the ridge axis instead most likely marks the western edge of the axial valley.

## 5.2 Mid-crust to uppermost mantle—below 6 km bsl

The entire crust is well constrained by the *LRDM* at a resolution of $5 \times 5 \times 2$ km. The ridge axis is particularly well revealed due to its systematically lower *P*-wave velocity than the surrounding crust at all depths (Figs 5, 7 and 8). The low $Vp$ zone is wider in between OCCs (e.g. Figs 5c and 7c) and narrower at the OCCs, mirroring the variation in width of the neovolcanic seafloor (Mallows & Searle 2012). The *LRDM* also shows that the region immediately south−southwest of the 1325 OCC has a higher $Vp$ (7.5 km s$^{-1}$) at 7.0 km bsl (Figs 5f and 7f), suggesting a thinner crust there (Fig. 9g) that is accommodated as a thinner lower crust (Fig. 9f) and a shallowing of the Moho (Fig. 9h), regardless of whether the Moho here is a distinct interface or the top of a transition zone (Peirce *et al.* 2019). The shape and depth of this region is well resolved by the inversion (Figs S6c and d) and correlates with a positive MBA (Fig. 9c and also noted by Smith *et al.* 2008; Mallows & Searle 2012).

As already noted, the 6.0 km s$^{-1}$ velocity contour coincides with a change in the vertical velocity gradient. Below this contour, the crust displays a smaller vertical gradient ($<1$ s$^{-1}$), with seismic velocity ranging between 6.0 and 7.0 km s$^{-1}$ (Fig. 10). Such a seismic velocity and velocity gradient are characteristic of oceanic crust layer 3, postulated to be mainly composed of gabbro, but which may also incorporate a component of mantle rocks (Cannat *et al.* 1995; Dunn *et al.* 2017). Therefore, we use the 6.0 km s$^{-1}$ contour as a proxy for the upper-to-lower magmatic crustal transition; it is also associated with lower degrees of melting and the effect of deep hydrothermal circulation (Karson *et al.* 1987; Detrick *et al.* 1994; Schlindwein & Schmid 2016).

Analysis of 1-D velocity–depth profiles (Fig. 10) reveals that for subseafloor depths $>3$ km, the 1330 OCC has a slower velocity than all other OCCs located on the west flank with it instead displaying a greater similarity to the ridge axis and the eastern ridge flank. Furthermore, the inward-facing fault and inter-OCC deep basin (located in Fig. 9a) have similar 1-D velocity–depth structures to each other. All of the 1-D profiles converge to ∼7.5 km s$^{-1}$ at depth, which Peirce *et al.* (2019) demonstrate is a good proxy for the crust–mantle boundary at 13°N. Therefore, the average regional crustal thickness in the 13°N study area is ∼6 km (Fig. 9g), with a thinner section associated with the western-most deep lava-floored basin (centred at 29,30 model $x,y$) in between OCCs (∼5 km) and a thicker section at ridge axis (∼7 km). The $Vp$ gradient shows that, away from the OCCs, mid-crustal depths are characterized by clear ridge-parallel structures (e.g. Fig. 6f) which are interpreted to reflect inward-facing rotated fault blocks and, thus, crust resulting from more magmatic crustal formation processes.

The nature of the crust–mantle boundary is variable throughout the *LRDM*, with occasional, isolated sections displaying a high vertical velocity gradient that suggests a distinct Moho interface. Furthermore, the rarely observed PmP arrivals (Fig. 4) seem to correspond to ridge axis and inter-OCC settings, and to the thinner crust/shallower Moho region located in the southwest of the 3-D grid footprint (Fig. 6a). The location of the base of crust PmP reflection points, when compared to a map of Moho depth derived from the 7.5 km s$^{-1}$ contour (Fig. 9h), shows that these arrivals correlate with crust with a seabed morphology and/or subseabed velocity structure normally expected to result from magmatic accretion.
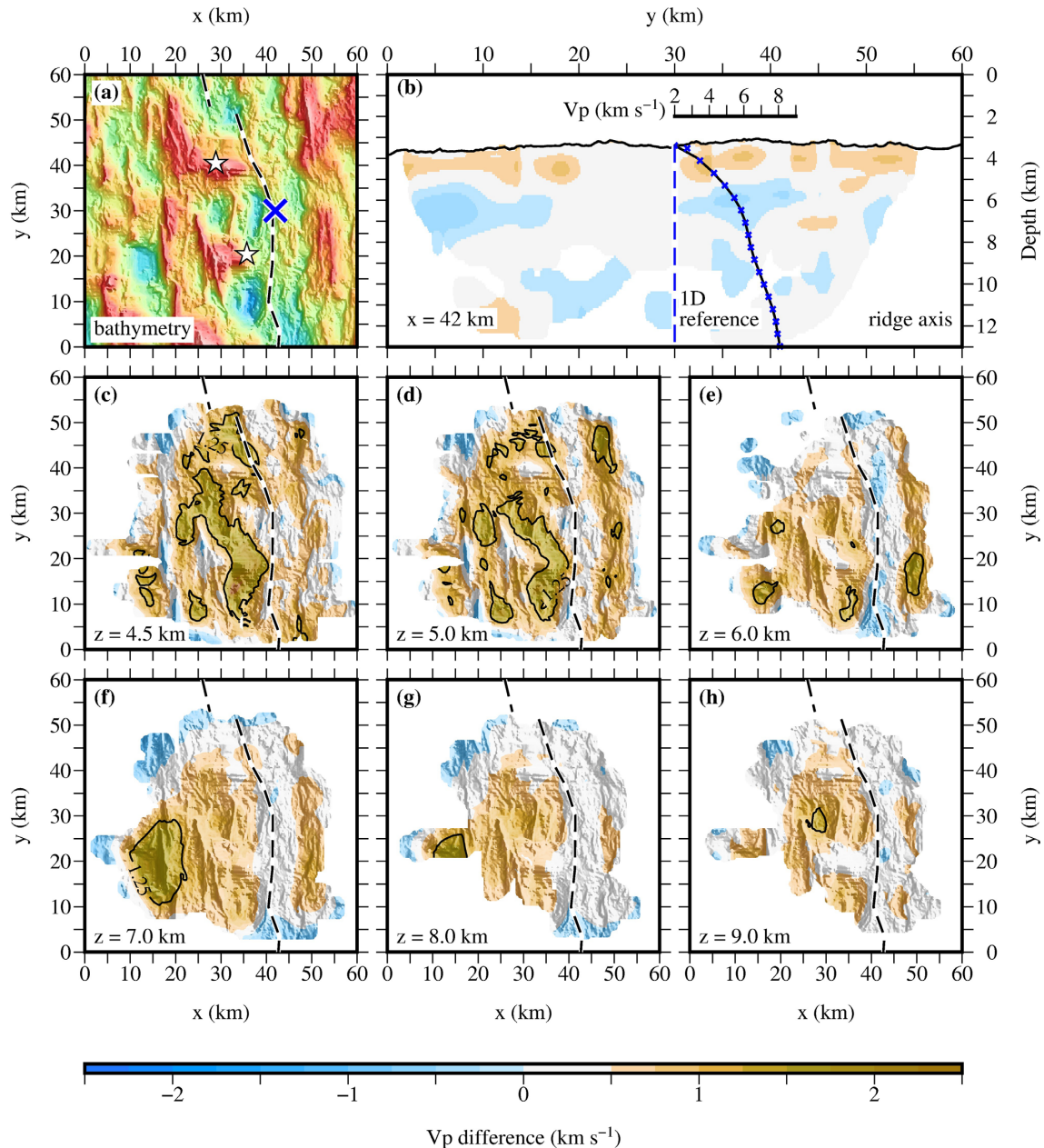
**Figure 7.** Horizontal (depth) slices through the inversion *HRSM* and *LRDM* plotted as the difference between the *inversion model* and the *reference model* constructed using a 1-D velocity–depth profile located in a region of the ridge axis thought to be magmatically spreading. See text for details of model construction. (a) Bathymetry showing the location of Mallows & Searle's (2012) average ridge axis (black dashed line in all parts) and the vent sites (white stars). Blue cross shows the 1-D reference profile location ($x = 42$ km, $y = 30$ km). (b) Vertical slice along axis (at model $x = 42$ km) approximately following Mallows & Searle's (2012) average ridge axis definition. The 1-D reference profile is shown with its location marked by the blue dashed line. Within inversion resolution, the ridge axis appears to have a velocity–depth structure expected for crust undergoing magmatic accretion. *Difference model* slices at (c) 4.5 km, (d) 5.0 km and (e) 6.0 km bsl through the *HRSM*, and at (f) 7.0 km, (g) 8.0 km and (h) 9.0 km bsl through the *LRDM*. The $+1.25$ km s$^{-1}$ contour is used as a proxy to demark the lateral and depth extent of the 1320, 1325 and 1330 OCCs in all parts. The ridge axis is highlighted by a north–south trending band of lower velocity that extends into the upper mantle (8.0 km and 9.0 km bsl slices). Parts (c–h) are masked by the *inversion model* ray coverage and are illuminated by the seabed topography. An unilluminated version of this figure is provided as Fig. S8.

## 5.3 OCCs

### 5.3.1 P-wave velocity structure

The analysis of 1-D profiles (Fig. 10) sampled from the 3-D grid at locations within each OCC (Fig. 9a) reveals that the shallowest (<2 km subseafloor depth) parts of the OCCs have a higher *Vp*
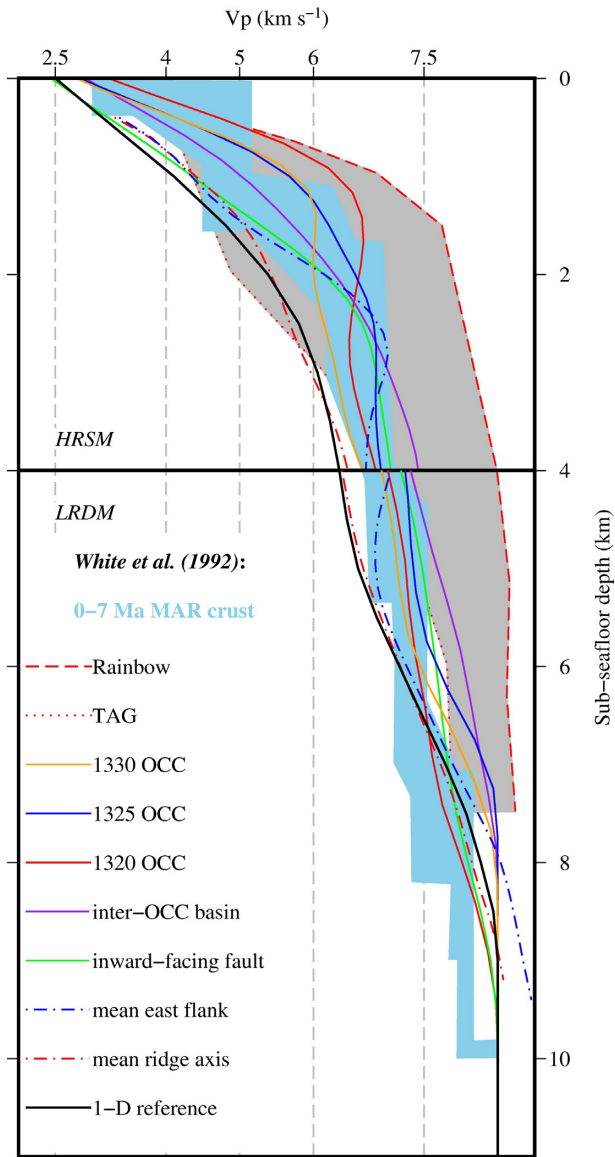
than all the other regional features. The observed velocities are, furthermore, all higher than White *et al.*'s (1992) average for 0–7 Ma MAR crust, and lie closer to those observed at the Rainbow vent field (Dunn *et al.* 2017) than those observed at TAG (Canales *et al.* 2007). The 1320 OCC has a higher upper crustal velocity than either of the 1325 or 1330 OCCs, both of which have similar profiles over this depth range.
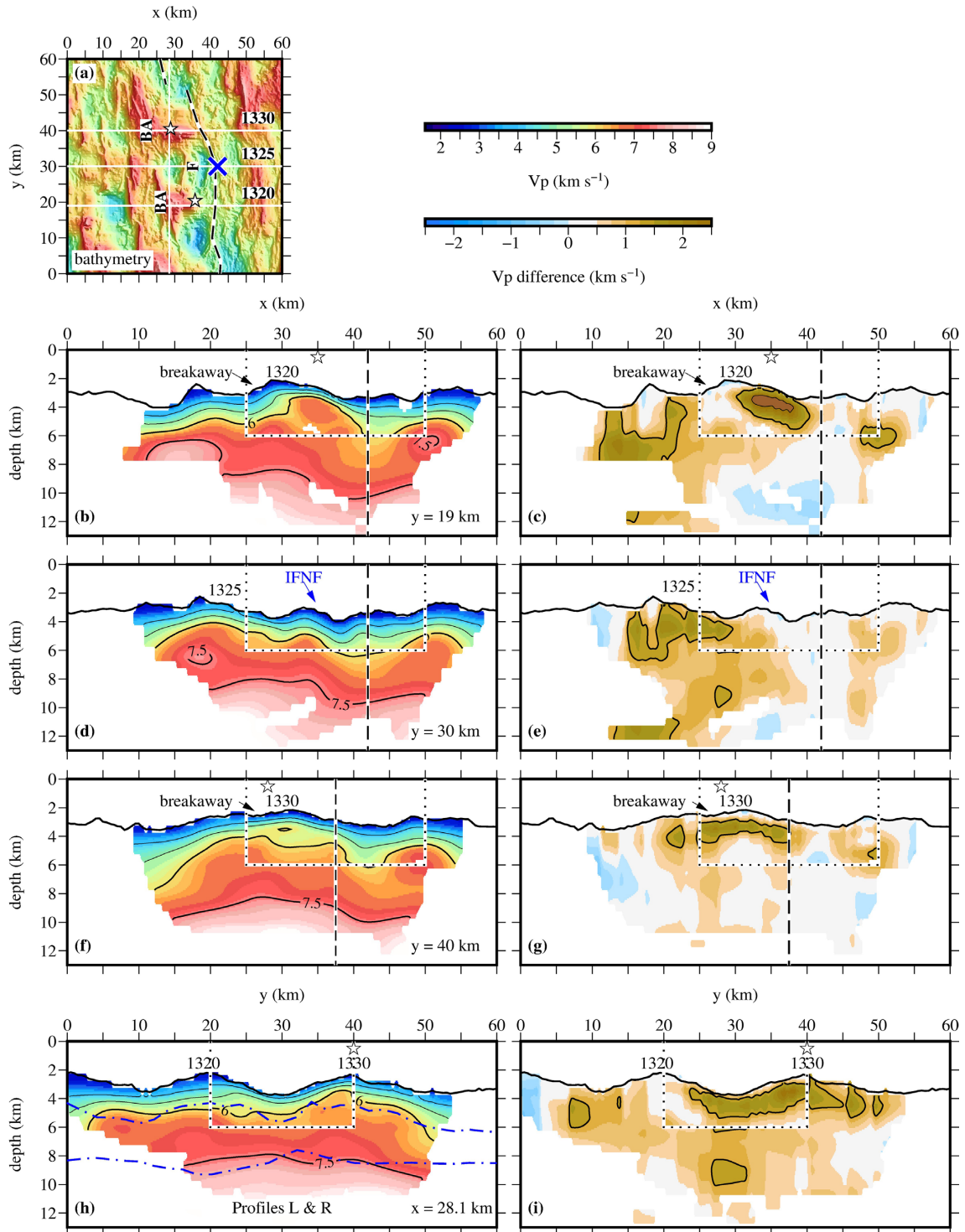
**Figure 8.** Vertical slices through the *inversion model*. (a) Bathymetry showing the location of Mallows & Searle's (2012) average ridge axis (black dashed line in all parts) and the vent sites (white stars). The 1320 and 1330 OCC breakaways (BA) and inward-facing normal fault (F) in between are marked and the location of vertical slices are shown by solid white lines. Blue cross shows the 1-D reference profile location. (b) West–east vertical slice through the 1320 OCC showing the *P*-wave velocity. The black dotted line in all parts outlines the contribution of the *HRSM* to the *inversion model*. Velocity contours are plotted at 1 km s$^{-1}$ intervals up to 6 km s$^{-1}$. Thicker black contours denote the proxy for the upper-to-lower crustal transition (6 km s$^{-1}$) and the base of crust transition (7.5 km s$^{-1}$—after Peirce *et al.* 2019). (c) West–east vertical slice through the *difference model* for the 1320 OCC showing with the +1.25 km s$^{-1}$ thicker contour highlighting the lateral and vertical extent of the OCC. Contours are plotted at 1.25 km s$^{-1}$ intervals. (d–e) Equivalent for the 1325 OCC. Inward-facing normal fault (IFNF) highlighted in blue. (f–g) Equivalent for the 1330 OCC. (h–i) Ridge axis-parallel profiles through the 1320 and 1330 OCCs along Profile L that is coincident with Profile R of Peirce *et al.* (2019). The 6.0 and 7.5 km s$^{-1}$ contours, derived from the Profile R 2-D velocity model, are plotted as blue dashed–dotted lines and are consistent with those of the *inversion model*. Parts (b–i) are masked using the *inversion model* ray coverage.
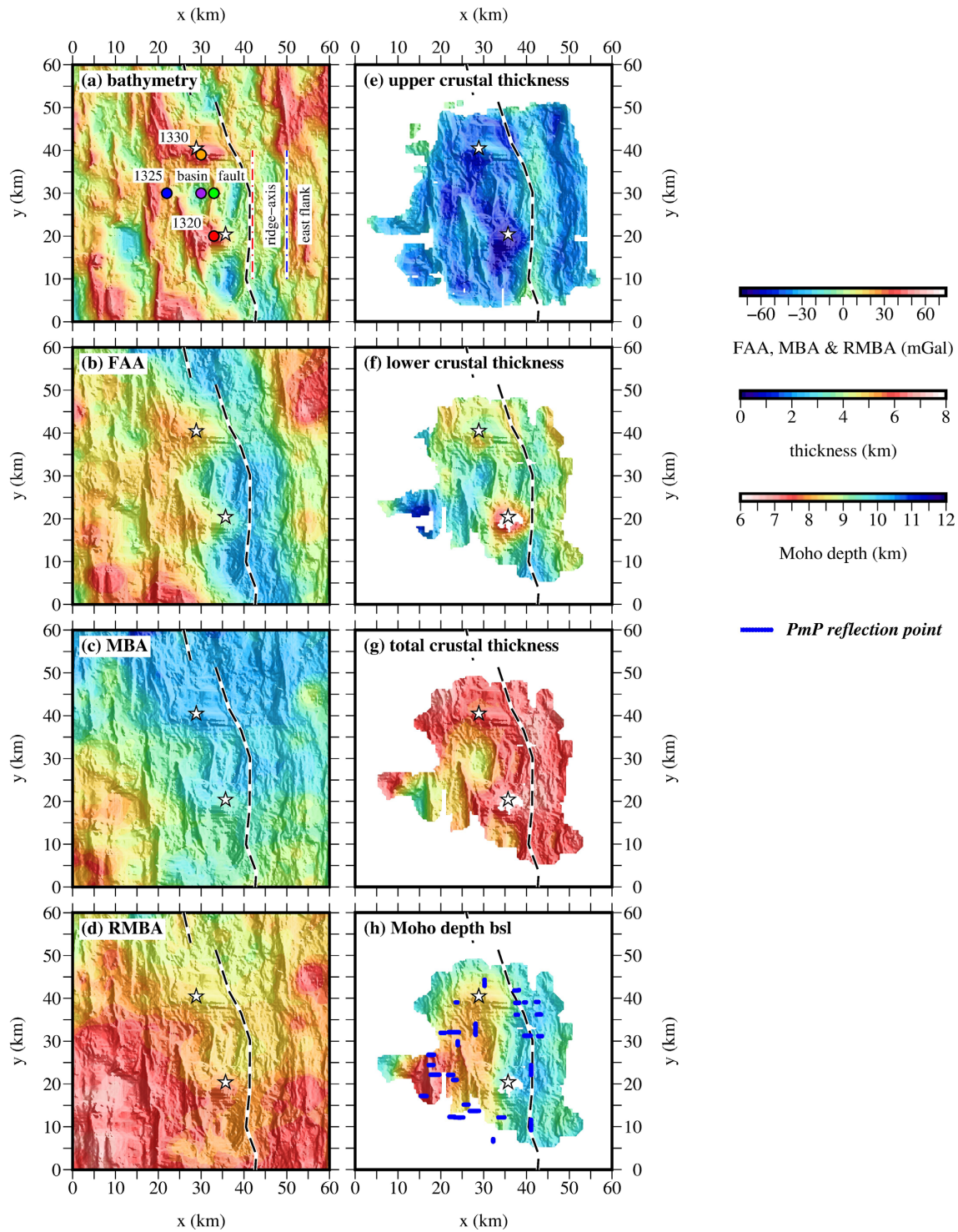
**Figure 9.** Layer thickness and gravity anomaly correlation. (a) Bathymetry showing the location of Mallows & Searle's (2012) average ridge axis (black dashed line in all parts) and the vent sites (white stars). The locations of 1-D velocity–depth profiles shown in Fig. 10 are marked by coloured circles. The locations of average 1-D velocity–depth profiles sampled along the ridge axis (red dotted–dashed line) and eastern ridge flank (black dashed–dotted line) are also highlighted. (b) Free-air anomaly (FAA) compiled from ship-based measurements made during JC102, JC109 and JC132 (Peirce 2014a, b; Reston & Peirce 2016). (c) Mantle Bouguer anomaly (MBA). (d) Residual mantle Bouguer anomaly (RMBA). All gravity anomalies were calculated following the approach outlined in Peirce *et al.* (2019). (e) Upper crustal thickness calculated using the depth to the 6.0 km s$^{-1}$ contour and subtracting the seabed depth shown in a). (f) Lower crustal thickness calculated by subtracting the bsl depth of the upper crustal surface (e) from the depth to base of crust surface (h). (g) Total crustal thickness variation throughout the 13°N 3-D grid footprint, as sum of (e) and (f). (h) Moho depth, calculated as the sum of seafloor depth plus depth bsl of the 7.5 km s$^{-1}$ contour. PmP reflection points calculated by 2-D forward ray-tracing (Fig. 4) are shown by blue lines in (h). Parts (e–h) are masked using the *inversion model* ray coverage and are illuminated by the seabed topography. An unilluminated version of this figure is provided as Fig. S9.

**Figure 10.** 1-D velocity–depth profiles of 1320, 1325 and 1330 OCCs, an inward-facing normal fault block, the ridge axis and the eastern ridge flank (see legend and Fig. 9a), compared with profiles for the TAG detachment (Canales *et al.* 2007) and the Rainbow massif (Dunn *et al.* 2017). The grey shading shows the velocity–depth range between the TAG and Rainbow locations. The average MAR crustal velocity–depth envelope of White *et al.* (1992) (light blue shading) is shown for reference.

A north–south trending vertical model slice through the 1320 and 1330 OCCs in the vicinity of the breakaway (Figs 8h and i) shows that the highest velocities are isolated beneath the topographic highs, and that these OCCs appear not to be connected, at least not at shallow-to-mid-crustal depth. This vertical slice lies along Profile R (Peirce *et al.* 2019) and a comparison of their 6.0 and 7.5 km s$^{-1}$ velocity contours with those of the *inversion model* shows that they are consistent despite the 2-D versus 3-D inversion approaches adopted (Fig. 8h).

The 1325 OCC is situated along a north–south band of relatively high velocity material ($x = 20$ km in Figs 5c and d) that correlates with a crustal magnetization positive anomaly (Smith *et al.* 2008; Mallows & Searle 2012). This OCC is also separated from the present-day active 1320 OCC by a region of lower velocity. This

lower velocity region coincides with a seafloor comprising rotated ridges, hummocky terrain and mafic horsts (Fig. 1c) that record a magmatic spreading period (MacLeod *et al.* 2009; Mallows & Searle 2012). In addition, the *HRSM* shows that the 1330 OCC has a higher velocity shallow crust extending from the ridge axis westwards towards the breakaway at ∼1.5 Ma off axis ($x ≈ 20$ km, Figs 5c–d and 8f–g). Checkerboard tests indicate that this variation in *Vp* is well resolved (S4c and d).

### 5.3.2 Detachment geometry and connectivity

Previous studies of mid-ocean ridges associate variation in seismic velocity with detachment faults (Canales *et al.* 2007; deMartin *et al.* 2007; Dunn *et al.* 2017). We use the +1.25 km s$^{-1}$ *Vp difference model* contour to demarcate the detachment surface with depth for both the 1320 (Fig. 11) and 1330 (Fig. 12) OCCs, in a similar manner to the approach adopted by deMartin *et al.* (2007). This contour coincides remarkably well with the location and dip of the shallower cluster of microseismicity observed to the south side of the 1320 OCC (Parnell-Turner *et al.* 2017—e.g. Fig. 11c). This correlation enables use of this proxy contour to map not only the detachment fault plane geometry with depth, but also test the likelihood of inter-OCC connectivity along axis as a result. On this basis, the 1320 (Fig. 11) and 1330 (Fig. 12) detachment fault planes extend to a depth of at least ∼7 km bsl (∼4 km beneath the seafloor).

The 1320 OCC detachment fault plane displays different geometries between its southern and northern flanks. The southern flank displays a fault dip as high as ∼55–60°, and is seismically active to shallowest crustal depths (Fig. 11c), while for the northern flank the detachment fault dips at ∼40–55° and does not show any shallow seismicity (Fig. 11b). There is also a correlation between observed seismicity at the 1320 OCC and the *Vp* anomaly, whereby intermediate depth events (>9 km bsl) associated with compressive stresses (Parnell-Turner *et al.* 2017) are observed below the high *Vp* anomaly (Fig. 11f), and deeper seismicity (>10 km bsl) is recorded at the ridge axis mirroring the lower *Vp* modelled there. Between OCCs, the inward-facing normal fault has a fault plane dipping at 40° (Figs 11h and 12g). However, to the north of the 13°N segment-bounding NTO, on the opposite ridge flank, the inward-facing normal fault dips at less than 30° (Fig. 12h). Both Figs 11(e), (i) and 12(e), (i) suggest that the OCCs are not interconnected, and that the NTO itself is a near-vertical structure within the crust. Analysis of the *Vp* gradient (Fig. 6) shows that not only does the crust surrounding the OCCs have a ridge axis-trending pattern, but also that the OCC detachments clearly persist for at least 2–3 km below seabed, until they intersect with the present-day ridge axis.

## 5.4 Ridge axis

Mallows & Searle (2012) define the ridge axis at 13°N (Fig. 1c) on the basis of a study using near-seabed side-scan sonar data together with topography, gravity and magnetic fields. However, the relatively low *P*-wave velocity structure of the *inversion model* suggests that the ridge axis within the crust in fact lies further to the east, particularly when viewed as *Vp* difference between *reference* and *inversion models* (Fig. 7). This lower velocity pattern persists throughout the crust and also suggests that the neovolcanic zone of the ridge axis is narrower at depth than at the seabed. The pattern in the upper-to-mid-crust also highlights crust likely formed by magmatic accretion in between OCCs (Figs 7c and d) and that the 1320 and 1330 OCC detachments extend across Mallows &
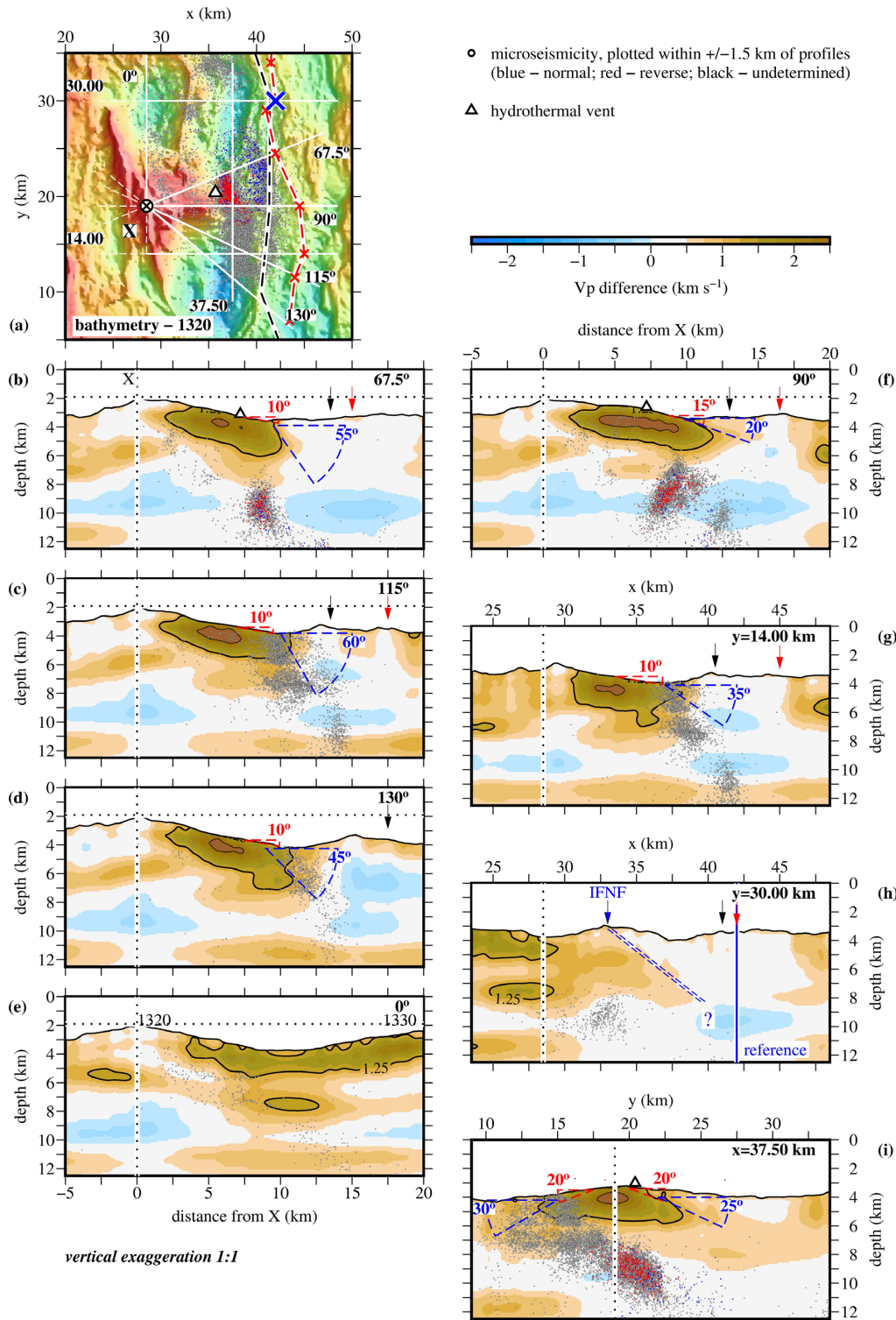
**Figure 11.** 1320 OCC detachment geometry. (a) Bathymetry surrounding the 1320 OCC with microseismic events (Parnell-Turner *et al.* 2017) coloured according to mechanism (see legend). White lines locate cross-sections shown in (b–i) with azimuths or *x,y* coordinates annotated in black. White triangle marks the Irinovskoe vent site in all relevant parts and the circled cross the intersection of each cross-section at the OCC (vertical dotted line in all other parts). Red dashed line marks the trend of the proposed ridge axis location based on the crustal structure derived from the *inversion model*. Mallows & Searle's (2012) average ridge axis is marked by the black dashed line. Blue cross shows the 1-D reference profile location. (b–i) Vertical cross-sections through the *difference model* for the *LRDM* at various azimuths, with earthquake hypocentres annotated. Sections are annotated in the top right corners by their azimuths (b–f) or are annotated by their *x* or *y* coordinate (g–i). Red arrows locate the proposed ridge axis further to the east, based on crustal velocity–depth structure; black arrows indicate the average ridge axis of Mallows & Searle (2012). Red and blue dashed wedges indicate the changing dip (annotated) of the detachment fault plane, based on the +1.25 km s$^{-1}$ velocity difference contour, on the exposed surface and at depth. Horizontal dotted line marks the shallowest depth of the 1320 OCC. IFNF—inward-facing normal fault.
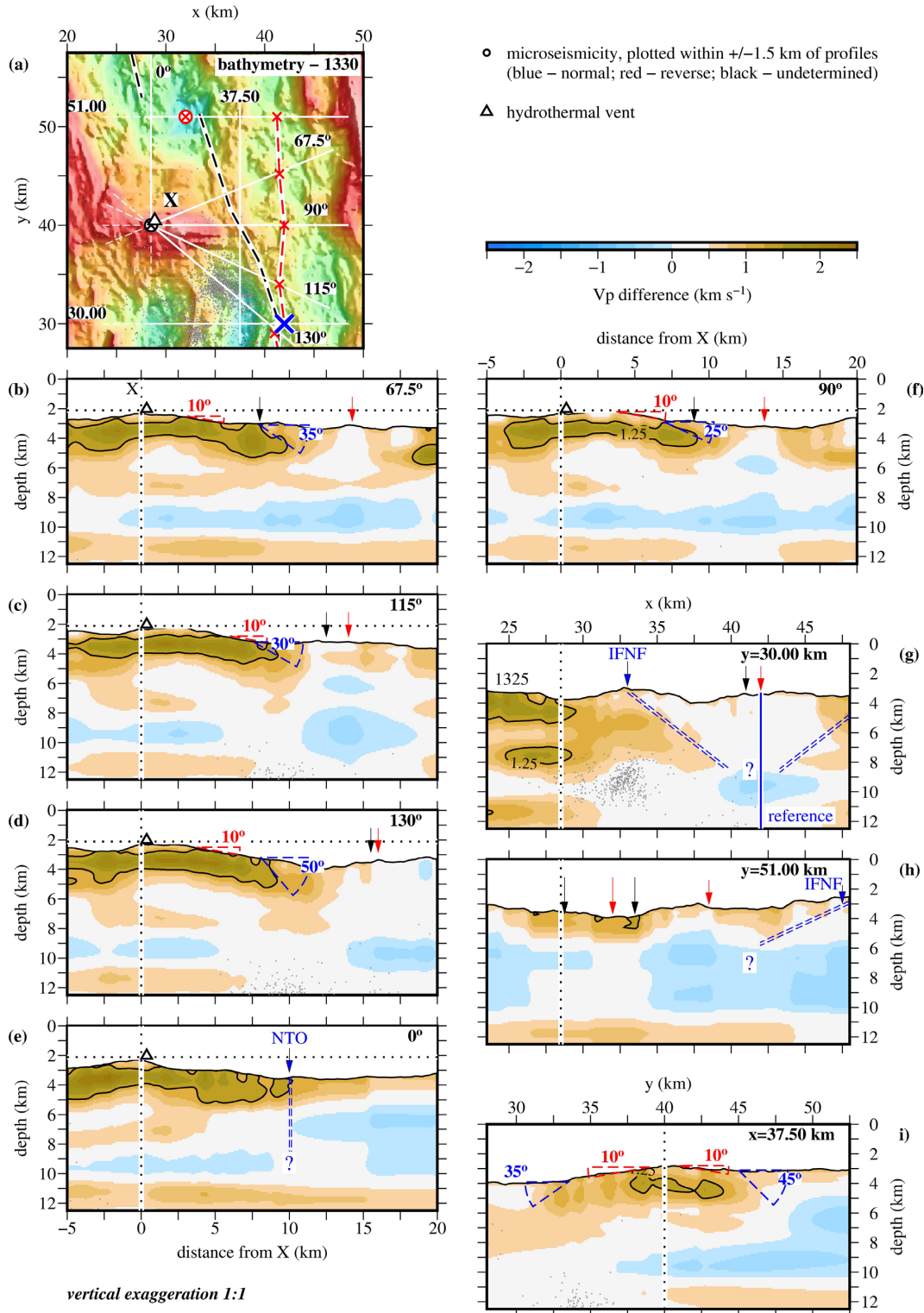
**Figure 12.** 1330 OCC detachment geometry. See Fig. 11 for details. The red circled cross in (a) marks the general location of the non-transform offset (NTO) shown in (e). White triangle marks the Semyenov vent site in all relevant parts.

Searle's (2012) average ridge axis with increasing depth subsurface (Figs 5d, e and 7d, e plan view; Figs 8, 11 and 12 vertical plane).

The vertical slice through the 1325 OCC also traverses the ridge axis (Fig. 8d), with the *difference model* [using the +1.25 km s$^{-1}$ Vp difference contour as an indicative proxy in a similar way to deMartin *et al.* (2007)–Fig. 8e] clearly indicating the presence of

lower velocity material within the axial region, bounded by inward-dipping fault-like features. For the vertical slices through the 1320 and 1330 OCCs (Figs 8c and g, respectively), a much narrower region of this material exists, and it is located further to the east than Mallows & Searle's (2012) average ridge axis location. Consequently, we conclude that the ridge axis lies up to 5 km further east,

and that the lower velocity regions could mark the foci of current magmatism.

The inward-facing normal fault crust on the western flank, the eastern ridge flank and the ridge axis itself have similar 1-D velocity structures (Fig. 10) to 2 km depth subseabed. The two basins between OCCs have a velocity structure comparable to the ridge-like structure that separates them, lying within White *et al.*'s (1992) envelope. This suggests that these are inward-facing fault block structures within sections of normal magmatically spread crust.

## 5.5 Hydrothermal vents

The two active vents, Semyenov and Irinovskoe (Fig. 1) are located in different settings on the 1320 and 1330 OCCs. In both cases, the seismic velocity models (Figs 4, 5, 7, 8, 11 and 12) show that there is no apparent velocity anomaly underlying each vent site within model resolution constraints. The resolution tests reveal that $2 \times 2 \times 1$-km-sized anomalies with velocity perturbations as low as 5 per cent of the surrounding crust should be well resolved to a subseafloor depth of ~1 km. Thus, if a heat source for Irinovskoe vent site is situated immediately beneath it, it is quite spatially restricted and/or limited in thermal/velocity contrast to its surrounds. If located between 1–4 km depth, any heat source would need to be smaller than $3 \times 3 \times 1$ km. Analogous observations can be made for the 1330 OCC where the source for the Semyenov vent site would have to be smaller than $3 \times 3 \times 1$ km if situated in the shallower part of the OCC and smaller than $5 \times 5 \times 1$ km if at mid-crustal depth.

## 6  DISCUSSION

Seismic tomography-derived models are smooth and interface free and, as such, structures are primarily defined by velocity contours and the rate of velocity change either with depth or laterally. To fully understand the 13°N 3-D *inversion model* thus requires consideration of the complex regional setting to distinguish between the effects, for example, of composition, porosity and temperature; all of which influence the propagation of seismic waves through the subsurface. We will now discuss our findings in the context of the variety of other relevant studies throughout the region which have used seismic (Peirce *et al.* 2019), gravity (Mallows & Searle 2012; Peirce *et al.* 2019), seismicity (Craig & Parnell-Turner 2017; Parnell-Turner *et al.* 2017), seafloor echo sounding and sonar backscatter (Smith *et al.*, 2006, 2008; MacLeod *et al.* 2009; Mallows & Searle 2012; Escartín *et al.* 2017; Parnell-Turner *et al.* 2018a, b; Olive *et al.* 2019) and seafloor sampling (MacLeod *et al.* 2009; Wilson *et al.* 2013; Bonnemains *et al.* 2017; Escartín *et al.* 2017) approaches to determine lithology, morphology and structural evolution.

### 6.1 Crustal structure

Subseafloor variation in density throughout the 13°N region is demonstrated by the free-air anomaly (FAA–Fig. 9b), the MBA (Fig. 9c) and to a lesser extent the residual mantle Bouguer anomaly (RMBA–Fig. 9d) which were calculated from ship meter data acquired during JC102, JC109 and JC132 following the approach outlined in Peirce *et al.* (2019). A local minimum in the MBA is centred at the ridge axis between OCCs. As a decrease in MBA is normally interpreted to imply a supply of melt to the ridge, this suggests that this MBA minimum may mark the centre of a small-scale magmatic segment, with 1320 and 1330 located near its edges.

With the exception of the southwest part of the 3-D grid footprint, the crustal thickness varies by less than 1 km (Fig. 9g), assuming the 7.5 km s$^{-1}$ velocity contour as a proxy for the base of crust, regardless of its form. We interpret the MBA local minimum as most likely being associated with a decrease of crustal density associated with the thickening of the upper crust (Fig. 9e), corresponding to the relatively lower *P*-wave velocity observed along the ridge axis (Figs 5, 7b–f and 8e). These observations support a current magmatic episode.

We can compare a north–south oriented vertical slice through the *inversion model* along Profile L, with the northern section of the longer, coincident 2-D refraction profile, Profile R (Fig. 13—Peirce *et al.* 2019), which traverses the Ashadze OCC complex to the south, the breakaway of the 1320 OCC, the 1330 OCC and the regions in between these features (Fig. 1). Given that these models were independently derived using different approaches, they are remarkably consistent, thus allowing us to compare the crustal structure of the 1320 and 1330 OCCs imaged by the 13°N 3-D grid with the OCCs to the south. Both models reveal that the upper-to-lower crustal transition is deeper beneath the 1320 OCC breakaway (~2 km) than at the equivalent location beneath the other OCCs. Both the 2-D and 3-D models (Figs 13a and b) also reveal that, with the exception of the OCCs, the magmatic upper crust (layer 2) is ~2 km thick from the NTO in the north to the Marathon FZ in the south (Fig. 1). Therefore, a comparatively thinner upper crustal section associated with the OCCs seems to be a characteristic feature of those located on the west flank of this part of the MAR. The upper crustal thickness variations associated with the OCCs situated along the west flank suggests a magmatic control on their formation and ephemeral life cycle, with these locations marking a localized waning of the magma supply to the ridge axis.

Previous studies, interpreting across-ridge-axis 2-D density profiles, have proposed that the 1320 and 1330 OCCs display differing density structures (Mallows & Searle 2012). Both OCCs are proposed to comprise diabase and/or highly serpentinized peridotite-like densities in their hangingwalls, while the shallow part of the OCC footwall and the breakaway regions reveal densities normally associated with gabbros and/or serpentinized peridotites. The primary difference between these OCCs is that the 3-D grid *inversion model* suggests that the 1320 OCC has a larger portion of its deeper footwall composed of peridotites than the 1330 OCC. Similarly, the 2-D refraction and gravity modelling study along Profile R (Peirce *et al.* 2019) reveals the 1330 OCC to have a lower *P*-wave velocity and a less dense crust than the Ashadze OCCs, suggesting that the latter is more dominated by ultramafics. The 3-D grid *inversion model* also shows the 1330 OCC to have a lower seismic velocity, most probably reflecting magma intrusion across the NTO, perhaps due to southward ridge tip propagation from the adjacent 14°N segment (MacLeod *et al.* 2009).

Fig. 8 illustrates the differences in velocity–depth structure between a mature, active OCC (1320—Fig. 8b) and an effectively inactive OCC (1325 and 1330—Figs 8d and f, respectively). The thinning of the upper crust beneath the southern edge of the 1330 OCC (Fig. 8h) coincides with magmatic intrusions (MacLeod *et al.* 2009). Similar features are observed at the 13°48′N OCC (MacLeod *et al.* 2009; Parnell-Turner *et al.* 2018b). Both flanks of the 1330 OCC (Fig. 12i) show a steeper dip than the northern flank of the 1320 OCC to the south (Fig. 11i), with the south flank of the 1320 OCC and both flanks of the 1330 OCC showing a significant shallowing of the detachment as it rolls over within the shallower part of the crust. Such a steep dip and correspondence with magmatic intrusions suggests that, first, these OCCs are not interconnected and,
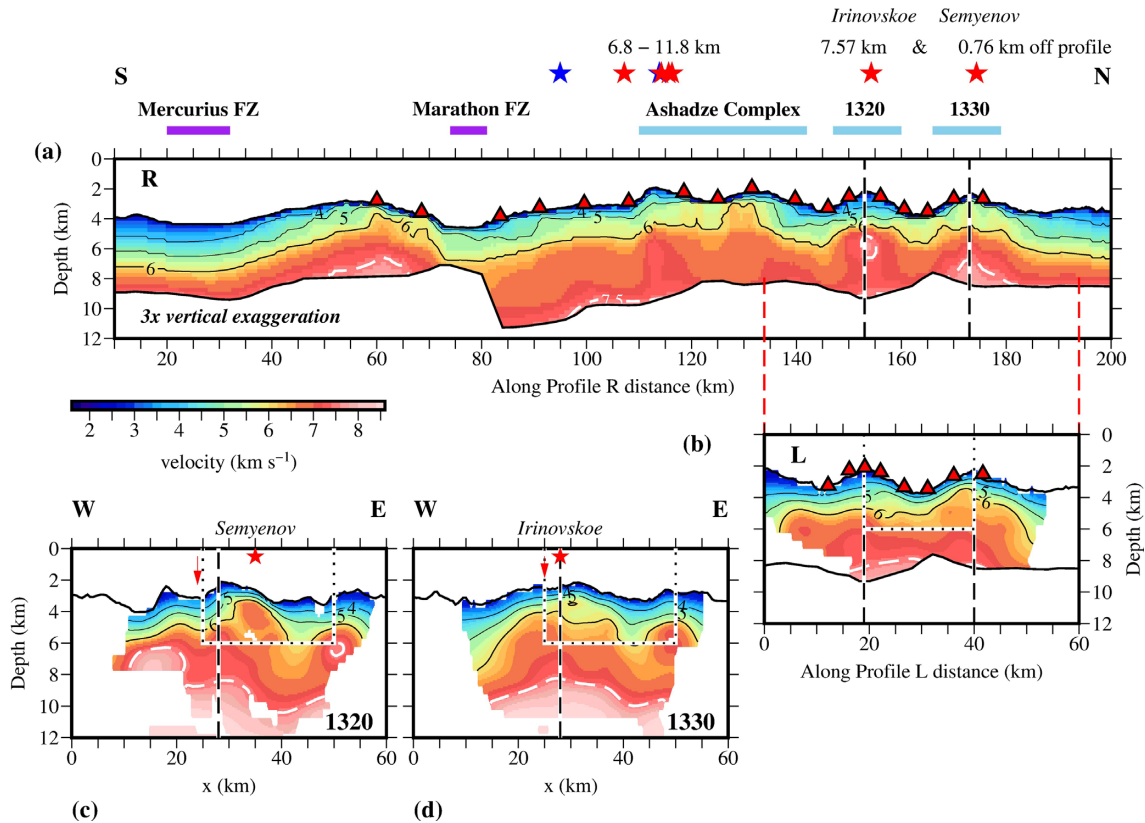
**Figure 13.** Comparison between velocity–depth models from Profile R (a), Profile L (b) and west-east sections through OCCs 1320 (c) and 1330 (d). (a) Peirce *et al.*'s (2019) 2-D velocity–depth model along Profile R with contours plotted at 1 km s$^{-1}$ intervals. The 6.0 km s$^{-1}$ contour acts as a proxy for the upper-to-lower crustal transition. The solid black line marks the base of crust transition resulting from combined inversion and forward seismic and gravity modelling. The 7.5 km s$^{-1}$ contour, on which the base of crust modelling was initially based, is shown as a white dashed line. (b) Profile L extracted from the 3-D grid *inversion model* of this study with red dashed lines showing its location along Profile R. Black dotted line shows the *HRSM* contribution to the *inversion model*. (c) Perpendicular (west-east) profile through the 1320 OCC showing the location of the breakaway (red arrow) and labelled vent site (red star). The intersection with Profiles L and R is marked by the vertical black dashed line. (d) Equivalent for the 1330 OCC. In both (c) and (d) the white dashed 7.5 km s$^{-1}$ contour acts as a proxy for the base of crust. Parts (b–d) are masked using the *inversion model* ray coverage.

second, that magmatism plays a role in the cessation of detachment faulting (Howell *et al.* 2019).

Smith *et al.* (2008) and Mallows & Searle (2012) note an increase in the MBA (Fig. 9c) in the southwest of the 13°N region. This coincides with an apparent thinning of the lower crust as shown by the *inversion model* (Fig. 9f). Correlations between amagmatic terrain, positive MBA and thinner crust have also been observed at the MAR near the 15°20′N FZ (e.g. Fujiwara *et al.* 2003). In both locations, the thinner crust is associated with irregular, oblique and rotated fault blocks and extensive outcrops of serpentinized peridotite (Fujiwara *et al.* 2003; Smith *et al.* 2008). In the southwest of the 13°N region, however, the inferred crustal thinning is located far from any known fracture zone. Consequently, this could reflect a past ridge jump, as it is mirrored by the parallel band of off axis seismicity recorded to the west (Escartín *et al.* 2003b—Fig. 1b).

Generally, the 7.5 km s$^{-1}$ velocity contour lies between 5 and 6 km-depth below seafloor (Fig. 8). Modelling of PmP arrivals shows that, where these phases are observed, they arise due to a step-wise change in velocity with depth, while elsewhere the transition from crust to mantle is gradual. A potential cause of this gradual change is lateral variation in magmatic process such that magma solidifies within the lithosphere as it ascends (Wilson *et al.* 2013; Dunn *et al.* 2017). This, in turn, leads to an increasing volume of crust-like material with depth (Cannat 1996; Kelemen *et al.* 2004).

Alternatively, detachments and normal spreading-related faulting facilitates fluid ingress into the crust, and potentially uppermost mantle. These fluids metamorphose the gabbros of the lower crust and peridotites of the upper mantle, in effect blurring the transition between the two in seismic velocity terms, and resulting in an irregular transition between mafic and ultramafic lithologies within the lower crust and upper mantle (Jarchow & Thompson 1989). These lithologies are ultimately exhumed at the seabed along a detachment over a geological time frame.

### 6.2 OCC fault geometry

Comparison between the 1320 OCC microseismicity and the *inversion model* (Fig. 11) reveals that there are three distinct regions defining the detachment fault surface, rather than the two previously inferred (Parnell-Turner *et al.* 2017). Parnell-Turner *et al.* (2017) equate the observed deep extensional earthquakes located close to the ridge axis to a steep fault zone at the base of the crust, whilst the intermediate-depth, compressional earthquakes are attributed to the build-up of stress in the footwall, due to fault bending roll-over to a lower angle as it reaches the seafloor. The rest of the detachment fault is considered to be slipping aseismically.

Our observations, however, indicate that the 3-D geometry of an OCC detachment fault is more complex than this (Figs 11 and 12).

For the 1320 OCC, the southern portion of the fault plane slips seismically at shallow depths (<5 km) beneath the seafloor, while the compressive seismicity is located immediately below the higher $V_p$ anomaly (>5 km) associated with the OCC (Figs 11b, f and i), and the deep (>10 km) microseismicity at the ridge axis is observed as a separate deeper cluster associated with the zone of lower velocity (Figs 11a–d, f–g).

Considering these observations together, the 1320 OCC detachment fault could be interpreted as having initiated within the upper crust along an alteration front, corresponding to the rheological boundary between weak and strong lithospheric sections, and where magmatic intrusions result in transient variations in the thermal structure that affect the depth of the brittle–ductile transition (Escartín *et al.* 2003a; Picazo *et al.* 2012). If this is the case, then the roll-hinge of the detachment fault lies at depth within the footwall, with the extensional seismicity instead relating to ridge spreading processes operating in the deeper crust and uppermost mantle (e.g. gabbro intrusion, etc.).

At the 1320 OCC, the detachment fault dip angle changes from steep- to low-angle over a distance of a few kilometres, with shallow earthquakes recorded along the steep southern flank (Fig. 11c), and little seismicity observed along the northern flank (Fig. 11i). Parnell-Turner *et al.* (2017) interpret the northern flank to be slipping aseismically due to anomalously low friction rheologies (Escartín *et al.*, 1997, 2003a; Picazo *et al.* 2012), and due to the low angle of faulting (Axen 1992; Sibson 1994). In the case of the 1320 OCC detachment fault plane, efficient strain localization caused by the rheology of quartz and basalt, which has been ubiquitously sampled (Bonnemains *et al.* 2017), suggests instead that factors such as pore fluids and effective confining pressure may be more important in controlling the effective friction along its shallowest depths before exhumation. High fluid pore pressures may be achieved in the fault plane by 'hangingwall overplating', as described by Bonnemains *et al.* (2017) and Escartín *et al.* (2017) at this OCC. Deep fluids at lithostatic pressure can be channelled into the brittle fault zone due to increased permeability caused by rupture. This high fluid pressure is maintained by low-permeability fine-grained mylonites below, and by mineralization and cemented breccia above, effectively sealing the system and inhibiting fluid circulation with the adjacent crust (Axen 1992; Sibson 1994).

The presence of silica-rich fluids and the widespread silicification of the detachment (Bonnemains *et al.* 2017) demonstrate that sustained hydrothermal circulation occurs, which once overpressured, can create the conditions for low-angle fault reactivation of high friction materials like quartz (Axen 1992; Sibson 1994). This reactivation would be impaired if slip is misaligned to the stress field (<<40°–Sibson 1994, 1996) which would explain the seismic quiescence observed in the concave down, low-angle section of the 1320 OCC detachment fault plane. Such a process would promote lock-slip instead of aseismic slip, and result in the medium-sized earthquakes which have been interpreted to occur in the shallowest part of the OCC (Craig & Parnell-Turner 2017). Either way, regardless of whether the OCC is aseismic or capable of producing medium-sized earthquakes, the strength of the fault plane itself varies between its southern (seismic) and northern (aseismic or lock-slip) flanks.

## 6.3 Faulting at 13°N on the MAR

The results of this study support the *local-scale* model of OCC development and evolution and the implications that model has for faulting processes (MacLeod *et al.* 2009). The rapid thinning of the shallower crust across OCCs (Figs 8h and i) reflects a disparity in tectonic heave between each OCC and the opposite flank of the ridge axis (MacLeod *et al.* 2009) that is not present elsewhere within the 13°N region. The thinning of the shallower crust across OCCs also coincides with locations of low backscatter terrain at the ridge axis, in contrast to the high backscatter volcanic terrain found throughout the rest of the region (Mallows & Searle 2012). The shallower crust is also thinner across the Ashadze OCCs located to the south (Peirce *et al.* 2019).

There is strong evidence to suggest that the 1320 and 1330 OCCs are at different stages of their respective life cycles. A 1-D velocity–depth profile through the 1330 OCC (Fig. 10) reveals significantly lower velocity at equivalent subseabed depth than the 1320 OCC. This reinforces the hypothesis that the northern OCC is coming to the end of its life cycle and may currently be being intruded by magma originating across the NTO to the north, as a result of southwards propagation of the 14°N segment ridge tip (MacLeod *et al.* 2009; Mallows & Searle 2012; Peirce *et al.* 2019).

Further evidence for the OCCs being in different stages of their life cycle is the contrasting detachment fault steepness (Figs 11 and 12). The 1330 OCC shows low-angle dips throughout its fault plane that may imply that it is at a later stage of exhumation. In contrast, the southern flank of the 1320 OCC has a steeper detachment fault plane, and the associated seismicity suggests that it is active and still exhuming material from deeper parts of the crust. Howell *et al.* (2019) postulate that waxing and waning magmatism controls detachment initiation and decline, with associated progressive fault rotation eventually being sufficient to result in lock-up in the subsurface (Buck 1988; Sibson 1994).

The Reston & Ranero (2011) *segment-scale* detachment fault model, in which normal fault rider blocks rafted from the hangingwall overlie an undulating single detachment surface along the entire segment length, does not fit the observations at 13°N. The evidence to support this conclusion is twofold: (1) the crustal structure between the 1320 and 1330 OCCs is equivalent to that on the eastern ridge flank and (2) the north–south ridge-like structure (at $x = 37$, $y = 46$–52 km) sits atop a steep normal-fault-like structure that separates shallow, higher velocity crust to the west from more normal oceanic crust to the east (where active volcanic structures are observed on the seabed). This ridge-like structure is interpreted as a relic inward-facing normal fault.

However, along-axis continuity between these OCCs may take the form of an interconnected network of different modes of faulting. Recent 3-D geodynamic modelling demonstrated that, even with an intermediate-to-high magma supply, transition zones between different modes of faulting are possible if a section of a fault weakens at a slower rate than in adjacent sections (Tian & Choi 2017; Howell *et al.* 2019). The correlation in patterns of microseismicity with fault geometry and depth, from seismic to aseismic (or lock-slip of large earthquakes), demonstrates that the strength of the 1320 OCC detachment is variable. Therefore, the 1320 OCC seems to be at the border of a transition between two types of faulting. As a consequence, it cannot be the surface expression of a detachment that also contains the 1330 OCC, but it can be a transfer zone between normal and detachment faulting. Conversely, 1330 OCC lies in the inside corner of a non-transform offset (this work and MacLeod *et al.* 2009; Mallows & Searle 2012; Peirce *et al.* 2019), which could suggest that OCCs originate as a result of the transfer between different modes of faulting and, thus, promote the coalescence of a network of linked fractures, where brittle deformation is

localized to relatively limited portions of the crust (Parnell-Turner *et al.* 2018a).

# 7 CONCLUSIONS

This 3-D seismic tomography study of the 13°N segment of the MAR aimed to investigate the crustal structure and inter-relationships between OCCs, and so investigate along axis connectivity of the associated detachment fault. It also aimed to provide a better understanding of magmatic and faulting processes associated with crustal formation at slower-spreading rates. From our study, we draw the following conclusions:

(i) on average, throughout the 13°N region, the crust is ∼6 km thick;

(ii) beneath the deep lava-floored basin in between OCCs the crust is thinner (∼5 km) and is more characteristically magmatic in layering and velocity–depth structure;

(iii) at the ridge axis the crust is relatively thicker (∼7 km) and coincides with lower *P*-wave velocities that suggest it is currently in a more magmatic phase of crustal formation;

(iv) the crust to the south of the 1325 and west of the 1320 OCCs is unusually thin (<4 km), which explains its corresponding anomalously high MBA and

(v) the crust–mantle boundary is a transition zone throughout most of the 13°N segment, except in isolated locations that also demonstrate magmatic characteristics.

Our 3-D grid tomographic results support the *local-scale* hypothesis (MacLeod *et al.* 2009) in which OCCs are associated with independent detachment faults which result in asymmetric spreading across the ridge axis. We draw this conclusion based on the following observations:

(i) the largest variation in thickness of the upper crust is focused at each OCC;

(ii) OCC bounding faults display significant relative changes in dip;

(iii) the distribution of microseismicity implies separate features and

(iv) seabed morphology and sampling suggest that the 1320 and 1330 OCCs are at different stages of their life cycles.

Finally, the change in steepness of the fault along the northern flank of the 1320 OCC is located at a transfer zone between the different faulting regimes observed to its south and north. Consequently, instead of detachment faults which traverse the entire length of the segment (Reston & Ranero 2011) as the mechanism for segment-scale asymmetric spreading, we propose that any along-axis fault connectivity is more likely to occur by OCCs acting as transfer zones linking different modes of faulting. OCCs, initially formed at shallow crustal depths, breach the seafloor where there is a strong asymmetry in seafloor spreading as a result of variation in magma supply along the ridge which, in turn, influences the rate at which faults weaken. This weakening may not only influence the way in which detachments rotate and migrate off axis before becoming finally inactive, but it may also influence how, when and where new OCCs are created.

# REFERENCES

Axen, G.J., 1992. Pore pressure, stress increase, and fault weakening in low-angle normal faulting, *J. geophys. Res.,* **97,** 8979–8991.

Baines, A.G., Cheadle, M.J., John, B.E. & Schwartz, J.J., 2008. The rate of oceanic detachment faulting at Atlantis Bank, SW Indian Ridge, *Earth planet. Sci. Lett.,* **273,** 105–114.

Blackman, D.K., Cann, J.R., Janssen, B. & Smith, D.K., 1998. Origin of extensional core complexes: evidence from the Mid-Atlantic Ridge at Atlantis Fracture Zone, *J. geophys. Res.,* **103,** 21 315–21 333.

Bonatti, E., Peyve, A., Kepezhinskas, P., Kurentsova, N., Seyler, M., Skolotnev, S. & Udintsev, G., 1992. Upper mantle heterogeneity below the Mid-Atlantic Ridge, 0°-15° N, *J. geophys. Res.,* **97,** 4461–4476.

Bonnemains, D., Escartín, J., Mével, C., Mével, C. & Andreani, M., 2017. Pervasive silicification and hanging wall overplating along the 13°20′N oceanic detachment fault (Mid-Atlantic Ridge), *Geochem. Geophys. Geosyst.,* **18,** 2028–2053.

Buck, W.R., 1988. flexural rotation of normal faults, *Tectonics,* **7,** 959–973.

Buck, W.R., Lavier, L.L. & Poliakov, A.N.B., 2005. Modes of faulting at mid-ocean ridges, *Nature,* **434,** 719.

Canales, J.P., Sohn, R.A. & deMartin, B.J., 2007. Crustal structure of the Trans-Atlantic Geotraverse (TAG) segment (Mid-Atlantic Ridge, 26°10'N): implications for the nature of hydrothermal circulation and detachment faulting at slow spreading ridges, *Geochem. Geophys. Geosyst.,* **8,** Q08004, doi:10.1029/2007GC001629.

Canales, J.P., Tucholke, B.E. & Collins, J.A., 2004. Seismic reflection imaging of an oceanic detachment fault: Atlantis megamullion (Mid-Atlantic Ridge, 30°10'N), *Earth planet. Sci. Lett.,* **222,** 543–560.

Canales, J.P., Tucholke, B.E., Xu, M., Collins, J.A. & DuBois, D.L., 2008. Seismic evidence for large-scale compositional heterogeneity of oceanic core complexes, *Geochem. Geophys. Geosyst.,* **9,** Q08002, doi:10.1029/2008GC 002009.

Cann, J.R. *et al.*, 1997. Corrugated slip surfaces formed at ridge-transform intersections on the Mid-Atlantic Ridge, *Nature,* **385,** 329.

Cannat, M., 1993. Emplacement of mantle rocks in the seafloor at mid-ocean ridges, *J. geophys. Res.,* **98,** 4163–4172.

Cannat, M., 1996. How thick is the magmatic crust at slow spreading oceanic ridges?, *J. geophys. Res.,* **101,** 2847–2857.

Cannat, M., Lagabrielle, Y., Bougault, H., Casey, J., de Coutures, N., Dmitriev, L. & Fouquet, Y., 1997. Ultramafic and gabbroic exposures at the Mid-Atlantic Ridge: geological mapping in the 15° N region, *Tectonophysics,* **279,** 193–213.

Cannat, M., Mangeney, A., Ondréas, H., Fouquet, Y. & Normand, A., 2013. High-resolution bathymetry reveals contrasting landslide activity shaping the walls of the Mid-Atlantic Ridge axial valley, *Geochem. Geophys. Geosyst.,* **14,** 996–1011.

Cannat, M. *et al.*, 1995. Thin crust, ultramafic exposures, and rugged faulting patterns at the Mid-Atlantic Ridge (22°-24° N), *Geology,* **23,** 49–52.

Craig, T.J. & Parnell-Turner, R., 2017. Depth-varying seismogenesis on an oceanic detachment fault at 13°20′N on the Mid-Atlantic Ridge, *Earth planet. Sci. Lett.,* **479,** 60–70.

Dannowski, A., Grevemeyer, I., Ranero, C.R., Ceuleneer, G., Maia, M., Morgan, J.P. & Gente, P., 2010. Seismic structure of an oceanic core complex at the Mid-Atlantic Ridge, 22°19′N, *J. geophys. Res.,* **115,** B07106, doi:10.1029/2009JB006943.

deMartin, B.J., Sohn, R.A., Pablo Canales, J. & Humphris, S.E., 2007. Kinematics and geometry of active detachment faulting beneath the Trans-Atlantic Geotraverse (TAG) hydrothermal field on the Mid-Atlantic Ridge, *Geology,* **35,** 711–714.

Detrick, R., Collins, J., Stephen, R. & Swift, S., 1994. In situ evidence for the nature of the seismic Layer 2/3 boundary in oceanic crust, *Nature,* **370,** 288.

Detrick, R.S., Needham, H.D. & Renard, V., 1995. Gravity anomalies and crustal thickness variations along the Mid-Atlantic Ridge between 33° N and 40° N, *J. geophys. Res.,* **100,** 3767–3787.

Dick, H.J.B., Tivey, M.A. & Tucholke, B.E., 2008. Plutonic foundation of a slow-spreading ridge segment: oceanic core complex at Kane Megamullion, 23°30′N, 45°20′W, *Geochem. Geophys. Geosyst.,* **9,** Q05014.

Dosso, L., Hanan, B.B., Bougault, H., Schilling, J.G. & Jorone, J.-L., 1991. Sr Nd Pb geochemical morphology between 10° and 17° N on the Mid-Atlantic Ridge: a new MORB isotope signature, *Earth planet. Sci. Lett.,* **106,** 29–43.

Dunn, R.A., Arai, R., Eason, D.E., Canales, J.P. & Sohn, R.A., 2017. Three-dimensional seismic structure of the Mid-Atlantic Ridge: an investigation of tectonic, magmatic, and hydrothermal processes in the Rainbow area, *J. geophys. Res.,* **122,** 9580–9602.

Escartín, J. & Canales, J.P., 2011. Detachments in oceanic lithosphere: deformation, magmatism, fluid flow, and ecosystems, AGU Chapman conference on oceanic detachments, Agros, Cyprus, 8–15 May 2010, *EOS, Trans. Am. Geophys. Un.,* **92**(4), 31–32.

Escartín, J. & Cannat, M., 1999. Ultramafic exposures and the gravity signature of the lithosphere near the Fifteen-Twenty Fracture Zone (Mid-Atlantic Ridge, 14°-16.5° N), *Earth planet. Sci. Lett.,* **171,** 411–424.

Escartín, J., Hirth, G. & Evans, B., 1997. Effects of serpentinization on the lithospheric strength and the style of normal faulting at slow-spreading ridges, *Earth planet. Sci. Lett.,* **151,** 181–189.

Escartín, J., Mével, C., MacLeod, C.J. & McCaig, A.M., 2003a. Constraints on deformation conditions and the origin of oceanic detachments: the Mid-Atlantic Ridge core complex at 15°45′N, *Geochem. Geophys. Geosyst.,* **4,** 1067.

Escartín, J. *et al.*, 2017. Tectonic structure, evolution, and the nature of oceanic core complexes and their detachment fault zones (13°20′N and 13°30′N, Mid-Atlantic Ridge), *Geochem. Geophys. Geosyst.,* **18,** 1451–1482.

Escartín, J., Smith, D. & Cannat, M., 2003b. Parallel bands of seismicity at the Mid-Atlantic Ridge, 12–14° N, *Geophys. Res. Lett.,* **30,** 1620.

Escartín, J., Smith, D.K., Cann, J., Schouten, H., Langmuir, C.H. & Escrig, S., 2008. Central role of detachment faults in accretion of slow-spreading oceanic lithosphere, *Nature,* **455,** 790–794.

Früh-Green, G.L., Kelley, D.S., Bernasconi, S.M., Karson, J.A., Ludwig, K.A., Butterfield, D.A., Boschi, C. & Proskurowski, G., 2003. 30,000 years of hydrothermal activity at the Lost City vent field, *Science,* **301,** 495.

Fujiwara, T., Lin, J., Matsumoto, T., Kelemen, P.B., Tucholke, B.E. & Casey, J.F., 2003. Crustal evolution of the Mid-Atlantic Ridge near the Fifteen-Twenty Fracture Zone in the last 5 Ma, *Geochem. Geophys. Geosyst.,* **4,** doi:10.1029/2002GC000364.

Gràcia, E., Charlou, J.L., Radford-Knoery, J. & Parson, L., 2000. Non-transform offsets along the Mid-Atlantic Ridge south of the Azores (38° N-34° N): ultramafic exposures and hosting of hydrothermal vents, *Earth planet. Sci. Lett.,* **177,** 89–103.

Grevemeyer, I., Ranero, C.R. & Ivandic, M., 2018. Structure of oceanic crust and serpentinisation at subduction trenches, *Geosphere,* **14**(2), 1–23.

Grevemeyer, I., Reston, T.J. & Moeller, S., 2013. Microseismicity of the Mid-Atlantic Ridge at 7° S-8°15′S and at the Logatchev Massif oceanic core complex at 14°40′N-14°50′N, *Geochem. Geophys. Geosyst.,* **14,** 3532–3554.

Grimes, C.B., John, B.E., Cheadle, M.J. & Wooden, J.L., 2008. Protracted construction of gabbroic crust at a slow spreading ridge: constraints from

206 Pb/238 U zircon ages from Atlantis Massif and IODP hole U1309D (30° N, MAR), *Geochem. Geophys. Geosyst.,* **9,** Q08012.

Hansen, L.N. *et al.*, 2013. Mylonitic deformation at the Kane oceanic core complex: implications for the rheological behavior of oceanic detachment faults, *Geochem. Geophys. Geosyst.,* **14,** 3085–3108.

Hayman, N.W., Grindlay, N.R., Perfit, M.R., Mann, P., Leroy, S. & de Lépinay, B.M., 2011. Oceanic core complex development at the ultraslow spreading Mid-Cayman Spreading Center, *Geochem. Geophys. Geosyst.,* **12,** Q0AG02, doi:10.1029/2010GC003240.

Howell, S.M., Ito, G., Behn, M.D., Martinez, F., Olive, J.-A. & Escartín, J., 2016. Magmatic and tectonic extension at the Chile Ridge: evidence for mantle controls on ridge segmentation, *Geochem. Geophys. Geosyst.,* **17,** 2354–2373.

Howell, S.M., Olive, J.-O., Ito, G., Behn, M.D., Escartín, J. & Kaus, B., 2019. Seafloor expression of oceanic detachment faulting reflects gradients in mid-ocean ridge magma supply, *Earth planet. Sci. Lett.,* **516,** 176–189.

Ildefonse, B. *et al.*, 2007. Oceanic core complexes and crustal accretion at slow-spreading ridges, *Geology,* **35,** 623–626.

Jarchow, C.M. & Thompson, G.A., 1989. The nature of the Mohorovicic discontinuity, *Ann. Rev. Earth planet. Sci.,* **17,** 475–506.

Kelemen, P.B., Kikawa, E., Miller, J. *et al.* 2004. Igneous crystallization and localized deformation > 15 km beneath the Mid-Atlantic Ridge, 14–16 N, *Geochem. Cosmo. Acta,* **68**(11), A690.

Karson, J.A. *et al.*, 1987. Along-axis variations in seafloor spreading in the MARK area, *Nature,* **328,** 681.

Lagabrielle, Y., Bideau, D., Cannat, M., Karson, J.A. & MéVel, C., 1998. Ultramafic-mafic plutonic rock suites exposed along the Mid-Atlantic Ridge (10° N-30° N). Symmetrical-asymmetrical distribution and implications for seafloor spreading processes, in *Faulting and Magmatism at Mid-Ocean Ridges,* pp. 153–176, eds Buck, W.R. Delaney, P.T. Karson, J.A. & Lagabrielle, Y., American Geophysical Union, doi:10.1029/GM106p0153.

Lin, J., Purdy, G.M., Schouten, H., Sempere, J.-C. & Zervas, C., 1990. Evidence from gravity data for focused magmatic accretion along the Mid-Atlantic Ridge, *Nature,* **344,** 627–632.

MacLeod, C.J., Carlut, J., Escartín, J., Horen, H. & Morris, A., 2011. Quantitative constraint on footwall rotations at the 15°45′N oceanic core complex, Mid-Atlantic Ridge: implications for oceanic detachment fault processes, *Geochem. Geophys. Geosyst.,* **12,** Q0AG03, doi:10.1029/2011GC003503.

MacLeod, C.J. *et al.*, 2002. Direct geological evidence for oceanic detachment faulting: the Mid-Atlantic Ridge, 15°45′N, *Geology,* **30,** 879–882.

MacLeod, C.J. *et al.*, 2009. Life cycle of oceanic core complexes, *Earth planet. Sci. Lett.,* **287,** 333–344.

Mallows, C. & Searle, R.C., 2012. A geophysical study of oceanic core complexes and surrounding terrain, Mid-Atlantic Ridge 13° N-14° N, *Geochem. Geophys. Geosyst.,* **13,** Q0AG08, doi:10.1029/2012GC004075.

McCaig, A.M., Cliff, R.A., Escartín, J., Fallick, A.E. & Macleod, C.J., 2007. Oceanic detachment faults focus very large volumes of black smoker fluids, *Geology,* **35,** 935–938.

Miller, D.J. & Christensen, N.I., 1997. Seismic velocities of lower crustal and upper mantle rocks from the slow-spreading Mid-Atlantic Ridge, south of the Kane Transform Zone (MARK), *Proc. Ocean Drill. Program Sci. Results,* **153,** 437–454.

Minshull, T.A., Sinha, M.C. & Peirce, C., 2005. Multi-disciplinary, sub-seabed geophysical imaging, *Sea Technol.,* **46,** 27–31.

Morris, A., Gee, J.S., Pressling, N., John, B.E., MacLeod, C.J., Grimes, C.B. & Searle, R.C., 2009. Footwall rotation in an oceanic core complex quantified using reoriented Integrated Ocean Drilling Program core samples, *Earth planet. Sci. Lett.,* **287,** 217–228.

Ondréas, H., Cannat, M., Fouquet, Y. & Alain, N., 2012. Geological context and vents morphology of the ultramafic-hosted Ashadze hydrothermal areas (Mid-Atlantic Ridge 13° N), *Geochem. Geophys. Geosyst.,* **13,** Q0AG14, doi:10.1029/2012GC004433.

Ohara, Y., Yoshida, T., Kato, Y. & Kasuga, S., 2001. Giant megamullion in the Parece Vela Backarc Basin, *Mar. Geophys. Res.,* **22,** 47–61.

Okino, K., Matsuda, K., Christie, D.M., Nogi, Y. & Koizumi, K.-i., 2004. Development of oceanic detachment and asymmetric spreading at the Australian-Antarctic discordance, *Geochem. Geophys. Geosyst.,* **5,** doi:10.1029/ 2004GC000793.

Olive, J.-A., Behn, M.D. & Tucholke, B.E., 2010. The structure of oceanic core complexes controlled by the depth distribution of magma emplacement, *Nat. Geosci.,* **3,** 491–495.

Olive, J.-A., Parnell-Turner, R., Escartín, J., Smith, D.K. & Petersen, S., 2019. Controls on the seafloor exposure of detachment fault surfaces, *Earth planet. Sci. Lett.,* **506,** 381–387.

Parnell-Turner, R., Escartín, J., Olive, J.-A., Smith, D.K. & Petersen, S., 2018a. Genesis of corrugated fault surfaces by strain localization recorded at oceanic detachments, *Earth planet. Sci. Lett.,* **498,** 116–128.

Parnell-Turner, R., Mittelstaedt, E., Kurz, M.D., Jones, M.R., Soule, S.A., Klein, F., Wanless, V.D. & Fornari, D.J., 2018b. The final stages of slip and volcanism on an oceanic detachment fault at 13°48′N, Mid-Atlantic Ridge, *Geochem. Geophys. Geosyst.,* **19,** 3115–3127.

Parnell-Turner, R., Sohn, R.A., Peirce, C., Reston, T.J., MacLeod, C.J., Searle, R.C. & Simão, N., 2017. Oceanic detachment faults generate compression in extension, *Geology,* **45,** 923–926.

Peirce, C., 2014a. The role and detachment of faulting at slow-spreading mid-ocean ridges: RRS James Cook cruise report JC102, Durham University (unpublished), pp 19, https://www.bodc.ac.uk/resources/inventories/cruise_ inventory/reports/jc102.pdf.

Peirce, C., 2014b. The role and detachment of faulting at slow-spreading mid-ocean ridges: RRS James Cook cruise report JC109, Durham University (unpublished), pp 26, https://www.bodc.ac.uk/resources/inventories/cruise_ inventory/reports/jc109.pdf.

Peirce, C., Reveley, G., Robinson, A.H., Funnell, M.J., Searle, R.C., Simão, N.M., MacLeod, C.J. & Reston, T.J., 2019. Constraints on crustal structure of adjacent OCCs and segment boundaries at 13° N on the Mid-Atlantic Ridge, *Geophys. J. Int.,* **217**(2), 988–981.

Picazo, S., Cannat, M., Delacour, A., Escartín, J., Rouméjon, S. & Silantyev, S., 2012. Deformation associated with the denudation of mantle-derived rocks at the Mid-Atlantic Ridge 13°-15° N: the role of magmatic injections and hydrothermal alteration, *Geochem. Geophys. Geosyst.,* **13,** Q04G09, doi:10.1029/2012GC004121.

Planert, L., Flueh, E.R., Tilmann, F., Grevemeyer, I. & Reston, T.J., 2010. Crustal structure of a rifted oceanic core complex and its conjugate side at the MAR at 5° S: implications for melt extraction during detachment faulting and core complex formation, *Geophys. J. Int.,* **181,** 113–126.

Reston, T. & Peirce, C., 2016. The role and detachment of faulting at slow-spreading mid-ocean ridges: RRS James Cook cruise report JC132, Durham University (unpublished), pp 62, https://www.bodc.ac.uk/resources/invent-ories/cruise_inventory/reports/jc132.pdf.

Reston, T.J. & Ranero, C.R., 2011. The 3-D geometry of detachment faulting at mid-ocean ridges, *Geochem. Geophys. Geosyst.,* **12,** Q0AG05, doi:10.1029/2011GC003666.

Reston, T., Weinrebe, W., Grevemeyer, I., Flueh, E.R., Mitchell, N.C., Kirstein, L., Kopp, C. & Kopp, H., 2002. A rifted inside corner massif on the Mid-Atlantic Ridge at 5° S, *Earth planet. Sci. Lett.,* **200,** 255–269.

Sato, T., Okino, K. & Kumagai, H., 2009. Magnetic structure of an oceanic core complex at the southernmost Central Indian Ridge: analysis of shipboard and deep-sea three-component magnetometer data, *Geochem. Geophys. Geosyst.,* **10,** Q06003, doi:10.1029/2008GC002267.

Sauter, D. *et al.*, 2013. Continuous exhumation of mantle-derived rocks at the Southwest Indian Ridge for 11 million years, *Nat. Geosci.,* **6,** 314–320.

Schlindwein, V. & Schmid, F., 2016. Mid-ocean-ridge seismicity reveals extreme types of ocean lithosphere, *Nature,* **535,** 276–279.

Schouten, H., Smith, D.K., Cann, J.R. & Escartín, J., 2010. Tectonic versus magmatic extension in the presence of core complexes at slow-spreading ridges from a visualization of faulted seafloor topography, *Geology,* **38,** 615–618.

Searle, R.C., Cannat, M., Fujioka, K., Mével, C., Fujimoto, H., Bralee, A. & Parson, L., 2003. FUJI Dome: a large detachment fault near 64° E on the very slow-spreading Southwest Indian Ridge, *Geochem. Geophys. Geosyst.,* **4,** doi:10.1029/2003GC000519.

Searle, R.C., MacLeod, C.J., Peirce, C. & Reston, T.J., 2018. The Mid-Atlantic Ridge near 13°20′N: high-resolution magnetic and bathymetry imaging, *Geochem. Geophys. Geosyst.,* **20**(1), doi:10.1029/2018GC007940.

Searle, R.C., Tominaga, M., Peirce, C., Reston, T.J. & MacLeod, C.J., 2016. Near-bottom high resolution magnetic observation over and around an active oceanic core complex, MAR 13° N, T33A-2999, *Proceedings of the American Geophysical Union, Fall Meeting,* AGU, San Francisco.

Sibson, R.H., 1994. An assessment of field evidence for 'Byerlee' friction, *Pure appl. Geophys.,* **142,** 645–662.

Sibson, R.H., 1996. Structural permeability of fluid-driven fault-fracture meshes, *J. Struct. Geol.,* **18,** 1031–1042.

Simão, N., Escartín, J., Goslin, J., Haxel, J., Cannat, M. & Dziak, R., 2010. Regional seismicity of the Mid-Atlantic Ridge: observations from autonomous hydrophone arrays, *Geophys. J. Int.,* **183,** 1559–1578.

Smith, D.K., Escartín, J., Cannat, M., Tolstoy, M., Fox, C.G., Bohnenstiehl, D.R. & Bazin, S., 2003. Spatial and temporal distribution of seismicity along the norther Mid-Atlantic Ridge (15° N-35° N), *J. geophys. Res.,* **108,** B3, doi:10.1029/2002JB001964.

Smith, D.K., Cann, J.R. & Escartín, J., 2006. Widespread active detachment faulting and core complex formation near 13° N on the Mid-Atlantic Ridge, *Nature,* **442,** 440–443.

Smith, D.K., Escartín, J., Schouten, H. & Cann, J.R., 2008. Fault rotation and core complex formation: significant processes in seafloor formation at slow-spreading mid-ocean ridges (Mid-Atlantic Ridge, 13°-15° N), *Geochem. Geophys. Geosyst.,* **9,** Q03003, doi:10.1029/2007GC001699.

Thibaud, R., Gente, P. & Maia, M., 1998. A systematic analysis of the Mid-Atlantic Ridge morphology and gravity between 15° N and 40° N: constraints of the thermal structure, *J. geophys. Res.,* **103,** 24 223–24 243.

Tian, X. & Choi, E., 2017. Effects of axially variable diking rates on faulting at slow spreading mid-ocean ridges, *Earth planet. Sci. Lett.,* **458,** 14–21.

Tivey, M.A., Schouten, H. & Kleinrock, M.C., 2003. A near-bottom magnetic survey of the Mid-Atlantic Ridge axis at 26° N: implications for the tectonic evolution of the TAG segment, *J. geophys. Res.,* **108,** doi:10.1029/ 2002JB001967.

Tucholke, B.E. & Lin, J., 1994. A geological model for the structure of ridge segments in slow spreading ocean crust, *J. geophys. Res.,* **99,** 11 937–11 958.

Tucholke, B.E., Behn, M.D., Buck, W.R. & Lin, J., 2008. Role of melt supply in oceanic detachment faulting and formation of megamullions, *Geology,* **36,** 455–458.

Tucholke, B.E., Lin, J. & Kleinrock, M.C., 1998. Megamullions and mullion structures defining oceanic metamorphic core complexes on the Mid-Atlantic Ridge, *J. geophys. Res.,* **103,** 9857–9866.

Wessel, P., Smith, W.H.F., Scharroo, R., Luis, J. & Wobbe, F., 2013. Generic Mapping Tools: improved version released, *EOS, Trans. Am. Geophys. Un.,* **94,** 409–410.

White, R.S., McKenzie, D. & O'Nions, R.K., 1992. Oceanic crustal thickness from seismic measurements and rare earth element inversions, *J. geophys. Res.,* **97,** 19 683–19 715.

Wilson, S.C., Murton, B.J. & Taylor, R.N., 2013. Mantle composition controls the development of an oceanic core complex, *Geochem. Geophys. Geosyst.,* **14,** 979–995.

Zelt, C.A., 1998. Lateral velocity resolution from three-dimensional seismic refraction data, *Geophys. J. Int.,* **135,** 1101–1112.

Zelt, C.A. & Barton, P.J., 1998. Three-dimensional seismic refraction tomography: a comparison of two methods applied to data from the Faeroe Basin, *J. geophys. Res.,* **103,** 7187–7210.

Zelt, C.A. & Ellis, R.M., 1988. Practical and efficient ray tracing in two dimensional media for rapid traveltime and amplitude forward modelling, *Can. J. Explor. Geophys.,* **21,** 16–31.

Zelt, C.A. & Smith, R.B., 1992. Seismic traveltime inversion for 2-D crustal velocity structure, *Geophys. J. Int.,* **108,** 16–34.

## SUPPORTING INFORMATION

Supplementary data are available at GJI online.

**Figure S1.** Inversion modelling. (a) Range of initial models used for inversion. The starting point for inversion *HRSM* is marked in bold with red crosses showing the depths at which the velocity is defined. (b) Distribution of traveltime residuals for the 129824 first arrival traveltime picks modelled. (c) Traveltime residual plotted against shot-receiver offset, with red dashed lines marking the mean and standard deviation. (d)–(f) Equivalent for inversion *LRDM*.

**Figure S2.** Inversion modelling. Progression in $\chi^2$ fit and rms residual misfit through each of the six inversion iterations for the 100 defined starting models for both the (a) HRSM and (b) LRDM. The chosen initial model for each is highlighted in red. The statistics of fit of each inversion conducted using these initial models is annotated.

**Figure S3.** Horizontal (depth) slices through the inversion *HRSM* and *LRDM*. (a) Bathymetry showing the location of Mallows & Searle's (2012) average ridge axis (black dashed line in all parts) and the vent sites (white stars). (b) Vertical slice across axis through the initial model for 1320 OCC (at model $y = 20.0$ km) showing the 1-D velocity–depth structure starting point of the inversion of *HRSM*. The ridge axis is marked by the vertical black dashed line. Slices at (c) 4.5 km, (d) 5.0 km and (e) 6.0 km bsl through the *HRSM*, which has a resolution of $2 \times 2 \times 1$ km to a depth of ~5 km bsl and at (f) 7.0 km, (g) 8.0 km and (h) 9.0 km bsl through the *LRDM*, which has a resolution of $3 \times 3 \times 2$ km to a depth of ~7 km bsl. The 6.0 and 7.5 km s$^{-1}$ contours, used as proxies for the upper-to-lower crust and crust-to-mantle transitions, respectively, are shown by contour lines. The 1320, 1325 and 1330 OCCs correspond to higher velocity anomalies relative to the surrounding crust, and the ridge axis is marked by a north–south trending band of lower velocity. Parts (c–h) are masked using the *inversion model* ray coverage and have the outlines of the 1320 and 1330 OCCs marked by green lines. A version of this figure illuminated by the seabed topography is provided as Fig. 5.

**Figure S4.** Resolution testing of inversion *HRSM* for the horizontal slices in Figs 5(c)–(e). (a) Bathymetry showing the location of Mallows & Searle's (2012) average ridge axis (black dashed line in all parts) and the vent sites (white stars). (b) Applied $\pm 5$ per cent checkerboard velocity anomaly with $3 \times 3 \times 2$ km cell dimensions (vertical component not shown) that results in the best resolution achievable throughout the 13°N region for the upper crust. A $2 \times 2 \times 1$ km feature resolution is achievable in the centre of the 3-D grid due to the higher OBS density (inset). (c) Output checkerboard for a horizontal slice through the *HRSM* at 4.5 km bsl. (d) Average semblance. Inset shows the average semblance for the $2 \times 2 \times 1$ km checkerboard. (e and f) 5.0 km bsl depth slice and average semblance. (g and h) 6.0 km bsl depth slice and average semblance. Parts (c–h) are masked using the *inversion model* ray coverage and are illuminated by the seabed topography. An unilluminated version of this figure is provided as Fig. S5.

**Figure S5.** Resolution testing of inversion *HRSM* for the horizontal slices in Figs 5(c)–(e). (a) Bathymetry showing the location of Mallows & Searle's (2012) average ridge axis (black dashed line in all parts) and the vent sites (white stars). (b) Applied $\pm 5$ per cent checkerboard velocity anomaly with $3 \times 3 \times 2$ km cell dimensions (vertical component not shown) that results in the best resolution achievable throughout the 13°N region for the upper crust. A $2 \times 2 \times 1$ km feature resolution is achievable in the centre of the 3-D grid due to the higher OBS density (inset). (c) Output checkerboard for a horizontal slice through the *HRSM* at 4.5 km bsl. (d) Average

semblance. Inset shows the average semblance for the $2 \times 2 \times 1$ km checkerboard. (e and f) 5.0 km bsl depth slice and average semblance. (g and h) 6.0 km bsl depth slice and average semblance. Parts (c–h) are masked using the *inversion model* ray coverage and have the outlines of the 1320 and 1330 OCCs marked by green lines. A version of this figure illuminated by the seabed topography is provided as Fig. S4.

**Figure S6.** Resolution testing of inversion *LRDM* for the horizontal slices in Figs 5(f)–(h). (a) Bathymetry showing the location of Mallows & Searle's (2012) average ridge axis (black dashed line in all parts) and the vent sites (white stars). (b) Applied $\pm5$ per cent checkerboard velocity anomaly with $5 \times 5 \times 2$ km cell dimensions (vertical component not shown) that results in the best resolution achievable throughout the 13°N region within the crust and upper mantle. A $3 \times 3 \times 2$ km feature resolution is achievable in the centre of the 3-D grid due to the higher OBS density (inset). (c) Output checkerboard for a horizontal slice through the *LRDM* at 7.0 km bsl. (d) Average semblance. Inset shows the average semblance for the $3 \times 3 \times 2$ km checkerboard. (e–f) 8.0 km bsl depth slice and average semblance. (g–h) 9.0 km bsl depth slice and average semblance. Parts (c–h) are masked using the *inversion model* ray coverage and are illuminated by the seabed topography. An unilluminated version of this figure is provided as Fig. S7.

**Figure S7.** Resolution testing of inversion *LRDM* for the horizontal slices in Figs 5(f)–(h). (a) Bathymetry showing the location of Mallows & Searle's (2012) average ridge axis (black dashed line in all parts) and the vent sites (white stars). (b) Applied $\pm 5$ per cent checkerboard velocity anomaly with $5 \times 5 \times 2$ km cell dimensions (vertical component not shown) that results in the best resolution achievable throughout the 13°N region within the crust and upper mantle. A $3 \times 3 \times 2$ km feature resolution is achievable in the centre of the 3-D grid due to the higher OBS density (inset). (c) Output checkerboard for a horizontal slice through the *LRDM* at 7.0 km bsl. (d) Average semblance. Inset shows the average semblance for the $3 \times 3 \times 2$ km checkerboard. (e–f) 8.0 km bsl depth slice and average semblance. (g–h) 9.0 km bsl depth slice and average semblance. Parts (c–h) are masked using the *inversion model* ray coverage and have the outlines of the 1320 and 1330 OCCs marked by green lines. A version of this figure illuminated by the seabed topography is provided as Fig. S6.

**Figure S8.** Horizontal (depth) slices through the inversion *HRSM* and *LRDM* plotted as the difference between the *inversion model* and the *reference model* constructed using a 1-D velocity–depth profile located in a region of the ridge axis thought to be magmatically spreading. See text for details of model construction. (a) Bathymetry showing the location of Mallows & Searle's (2012) average ridge axis (black dashed line in all parts) and the vent sites (white stars). Blue cross shows the 1-D reference profile location ($x = 42$ km, $y = 30$ km). (b) Vertical slice along axis (at model $x = 42$ km) approximately following Mallows & Searle's (2012) average ridge axis definition. The 1-D reference profile is shown with its location marked by the blue dashed line. Within inversion resolution, the ridge axis appears to have a velocity–depth structure expected for crust undergoing magmatic accretion. *Difference model* slices at (c) 4.5 km, (d) 5.0 km and (e) 6.0 km bsl through the *HRSM*, and at (f) 7.0 km, (g) 8.0 km and (h) 9.0 km bsl through the *LRDM*. The $+1.25$ km s$^{-1}$ contour is used as a proxy to demark the lateral and depth extent of the 1320, 1325 and 1330 OCCs in all parts. The ridge axis is highlighted by a north–south trending band of lower velocity that extends into the upper mantle (8.0 and 9.0 km bsl slices). Parts (c–h) are masked by the *inversion model* ray coverage and have the outlines of the 1320 and 1330 OCCs marked by green

lines. A version of this figure illuminated by the seabed topography is provided as Fig. 7.

**Figure S9.** Layer thickness and gravity anomaly correlation. (a) Bathymetry showing the location of Mallows & Searle's (2012) average ridge axis (black dashed line in all parts) and the vent sites (white stars). The locations of 1-D velocity–depth profiles shown in Fig. 10 are marked by coloured circles. The locations of average 1-D velocity–depth profiles sampled along the ridge axis (red dotted–dashed line) and eastern ridge flank (black dashed–dotted line) are also highlighted. (b) Free-air anomaly (FAA) compiled from ship-based measurements made during JC102, JC109 and JC132 (Peirce 2014a, b; Reston & Peirce 2016). (c) Mantle Bouguer anomaly (MBA). (d) Residual mantle Bouguer anomaly (RMBA). All gravity anomalies were calculated following the approach outlined in Peirce *et al.* (2019). (e) Upper crustal thickness calculated using the depth to the 6.0 km s$^{-1}$ contour and subtracting the seabed depth shown in a). (f) Lower crustal thickness calculated by subtracting the bsl depth of the upper crustal surface (e) from the depth to base of crust surface (h). (g) Total crustal thickness variation throughout the 13°N 3-D grid footprint, as sum of (e) and (f). (h) Moho depth, calculated as the sum of seafloor depth plus depth bsl of the 7.5 km s$^{-1}$ contour. PmP reflection points calculated by 2-D forward ray tracing (Fig. 4) are shown by blue lines in (h). Parts (e–h) are masked using the *inversion model* ray coverage and have the outlines of the 1320 and 1330 OCCs marked by green lines. A version of this figure illuminated by the seabed topography is provided as Fig. 9.

Please note: Oxford University Press is not responsible for the content or functionality of any supporting materials supplied by the authors. Any queries (other than missing material) should be directed to the corresponding author for the paper.